Synthesis and Structure-dependent Properties of Novel Binary Nanoparticles

新規 2 元系ナノ粒子の合成と構造に依存した物性の評価

Md. Jafar Sharif

Hokkaido University
北海道大学

2013

Table of Contents

Chapter 1
General Introduction

1.1 Key Parameters for The Properties of Nanoparticles

Nanoparticles (NP) are defined as the materials having at least one dimension in the nanometer regime, typically less than 100 nm, which are considered as an intermediate between the atoms and the bulk. Over the last two decades, the NPs have been studied extensively due to their potential applicability in a variety of fields including catalysis, magnetism, opto-electronics, bio-medical and so on [1]. The NPs have aberrant features in electronic and geometric structures compared to bulk materials. The energy of electronic levels of NPs is quantized rather than continuous (bulk) because of the confinement effect in small spatial area. Therefore, the energy spacing in NPs can be regulated as a function of the sizes of the NPs. This fundamental difference in electronic structure induces metal to nonmetal transition in NPs. The geometric structures of metal NPs are also noticeably different from the bulk. NPs have high population of atoms with low coordination number due to the large number of atoms located at the surface. In addition, small NPs often possess non-close pack icosahedral structure. Because of this uniqueness in structures, NPs shows novel properties, which are not attainable in bulk materials. When the NPs are composed of a single component, their properties can be controlled by size and shape [2]. In contrast, if the NPs are composed of more than one component, other parameters such as composition and mixing mode can be used as key parameters to control the properties in addition to size and shape.

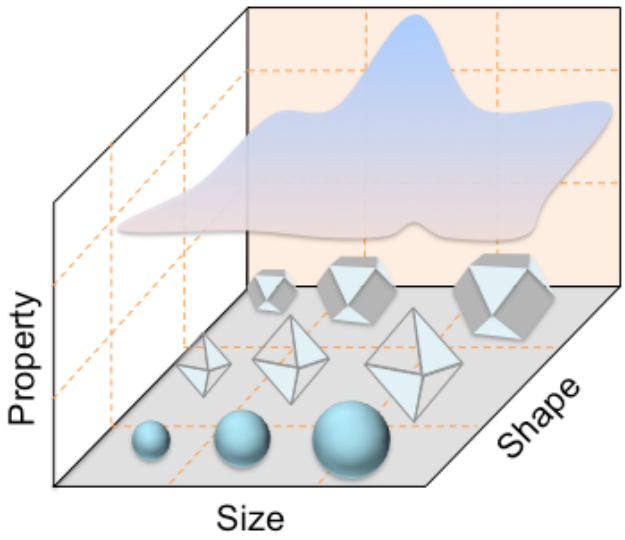

Figure 1.1. Typical dependency of size and shape on the properties of NPs.

1.1.1 Effect of Size

Among the all other structure parameters, size is the primary parameter for the NPs. Catalytic, magnetic, optical and thermodynamic properties of NPs can be tuned by changing the size. Tsunoyama *et al.* demonstrated the aerobic oxidation of benzyl alcohol by (poly(*N*-vinyl-2-pyrrolidone) (PVP) stabilized colloidal Au NPs [3]. The catalytic activity of Au NPs rapidly increased with decreasing size. The reverse trend in catalytic activity was observed in the aerobic oxidation of benzyl alcohol by PVP stabilized colloidal Pt NPs [4]. The selectivity of a reaction can also be tuned by changing the size of the catalyst. Kuhn *et al.* reported that the selectivity of pyrrole hydrogenation is strongly depended on the size of the dendrimer stabilized Pt NPs [5]. The selectivity to ring opening products is nearly 100 % for the Pt NPs larger than 2 nm. The origin of the size effects in catalysis is based on several factors: high surface/volume ratio; low coordination sites; quantum size effect.

For magnetic NPs, the size plays a crucial role in spin cross over, which induces an interesting phenomenon called super-paramagnetism. Super-paramagnetic materials can be defined as a class of ferromagnetic material in which the spin-up and spin-down states fluctuate frequently by the thermal energy of the material. Therefore, the net magnetization becomes zero and do not show any hysteresis behavior. The transition from ferromagnetism to super-paramagnetism is dependent on size. Another phenomenon related to ferromagnetism is the transition between single domain and multi domain. The general trend of size dependent magnetic properties is shown in Figure 1.1.

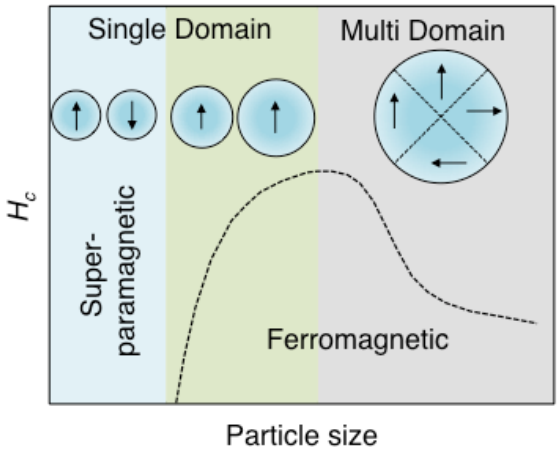

Figure 1.2. Size dependency on the magnetic behaviour of ferromagnetic materials.

1.1.2 Effect of Shape

Shape is the another important structure parameter to manipulate the properties of NPs. NPs of different shapes have been prepared by different method by changing several parameters such as concentration of precursor, type of stabilizer, type of reduction method etc. The catalytic properties of NPs were found to be dependent on the shape of the NPs. Bratlie *et al.* reported the shape

dependent hydrogenation of benzene by colloidal Pt NPs [6]. Narayanan *et al.* reported that the activation energy of electron transfer reaction between hexacyanoferrate ions and thiosulfate depend on the shape of Pt NPs of comparable size [7]. The origin of the shape dependent catalytic property was ascribed to terrace dependent activity of different products.

The magnetic properties are also strongly dependent on shape of the NPs. The main reason for this shape dependence is that the magnetic easy axis (axis of magnetization) depends on the geometry of the NPs. For a rod like shape the magnetic easy axis is determined by the aspect ratio. Nano rods with a high aspect ratio have an easy axis parallel to the long axis. Choi *et al.* investigated the magnetic properties by changing the aspect ratio of Co/Pt nano rod and found that the coercivity increases with the increase of the aspect ratio [8].

1.1.3 Effect of Composition

It has been established that the electronic structure of NPs is modified by the introducing secondary component and the modification is maximized for a specific composition. Charge transfer in NPs having two components with dissimilar electron affinity is the most pronounced modification in electronic structure. The geometric structure can also be modified by the addition of the second component because of the strain effects which ultimately change the bond distances of the NPs. The degree of overlapping between the orbitals decreases when the second component exerts tensile strain. Reverse modification is also possible if the second component produces compressive strain. Therefore, composition is another crucial parameter to control the properties of the NPs. Zhang *et al.* reported that Au decorated Pd NPs shows significant enhancement

in catalytic activity for the oxidation of glucose [9]. Chaki *et al.* reported the enhancement of catalytic activity for the oxidation of *p*-hydroxy benzyl alcohol by Ag doped Au NPs [10]. The origin of the enhancement in catalytic activity by these bimetallic NPs was ascribed to the intermetallic electron transfer [9,10]. In the above two examples, electron donation to Au atoms was observed.

In the case of magnetic property, the dopants can also modify the magnetic behavior drastically. Ito *et al.* reported that doping Fe or Co atoms could magnetize non-magnetic Pd NPs [11]. The magnetic moment becomes maximized at low concentration of Fe.

1.1.4 Effect of Mixing Mode

The mixing mode is an important parameter to control the properties of NPs since the extent of modification in electronic and geometric structure in binary NPs is dependent on the type of mixing mode. Therefore, in binary NPs, it is important to know how the two components are mixed in addition to size, shape or composition. The binary NPs can be categorized into mainly two types based on the mixing mode. The schematic representation of the classification is shown in Figure 1.2.

Single Phase: A single phase structure can be defined as homogeneously mixed solid solution structure where the atoms of the two different components occupy the different sites of a single type of crystal structure. Single-phase structure is usually formed between two metals. Solid solution bimetallic alloys such as Cu-Pd, Fe-Co, Fe-Pt are the examples of single-phase structure [12]. A single-phase structure can be further classified into two types.

Random structure: When the atoms of two different components occupy different sites of the crystal lattice by a random distribution method, the structure is defined as random structure. In a bcc CuPd alloy the two atoms are randomly distributed in the bcc structure.

Ordered structure: When the atoms of two different components occupy different sites of the crystal lattice by a sequential distribution method, the structure is defined as ordered structure. In a B2 CuPd alloy, the Cu atoms occupy the center position and the Pd atoms occupy the corner positions of the bcc structure [12(a)].

Two Phase: When two type of crystal structure present in a single material, the structure is defined as two phase structure. In two phase structure atoms of two components form a two individual crystal structure in two different area. Two-phase structure can be formed between metal-metal, metal-oxide and oxide-oxide. Rh-Cu in bulk state and Au@SiO_2 are the examples of two-phase structure [13, 14]. It can be further classified in to two classes.

Core-Shell structure: When one type of phase forms the core and the other type of phase forms the shell in a two phase system, the structure is defined as core-shell structure. A core-shell structure is usually written as A@B, where A is metal and B is either metal or oxide. Co@Pt, Au@SiO_2 are the examples of core-shell structures [14, 15].

Phase separated structure: When the two phases are separated by a phase boundary (grain boundary) into a two-phase system, the structure is defined as phase separated structure. A phase separated structure usually written as A/B, where A and B represent metal or oxide. The atoms of Rh and Cu in bulk state are not atomically mixed [13]. They form two different domains in two

different area of the alloy. Therefore, Rh-Cu in bulk state is an example of phase-separated structure.

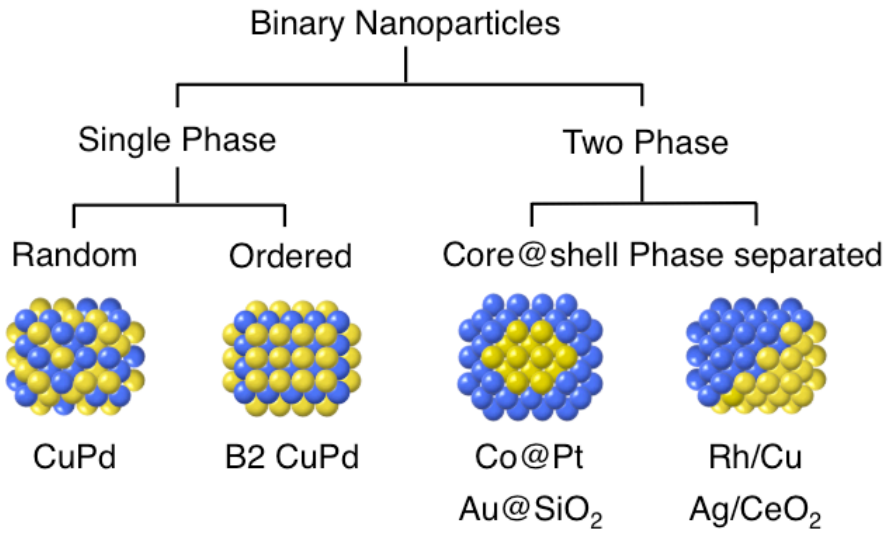

Figure 1.3. Classification of binary NPs. The blue and yellow spheres indicate the two different atoms.

There are few examples where the difference in property in two different mixing modes has been demonstrated. Kobayashi *et al.* demonstrated that the hydrogen storage property by Pd@Pt and PdPt nanoalloys (NAs) are strongly dependent on the mixing mode [16]. In the core shell Pd@Pt structure hydrogen can be stored only on the interfacial area of the core shell structure. Hydrogen storage is greatly enhanced in the solid solution PdPt structure.

Park *et al.* demonstrated the synthesis and magnetic properties of core shell and solid solution CoPt NAs [14]. For a core shell Co@Pt structure the magnetic properties are similar with monometallic Co NPs and shows coercivity of 300 Oe. The magnetic properties of solid solution CoPt are greatly enhanced and show large coercivity of 6900 Oe.

1.2 Aim of This Work

The aim of this work is to develop synthetic methods of novel binary NPs (metal-metal, metal-oxide) with controlled structure for the magnetic and catalytic properties. In this work, I mainly focused on controlled composition and mixing of two elements in binary NPs. However it is challenging to control the mixing mode in NPs. In order to mix two atoms homogeneously, heat treatment is required which induces sintering. On the other hand, all the metals are not miscible with each other. The immiscible metals cannot be mixed in a controlled way. To overcome these difficulties, I employed the following strategies.

1. Hydrogen can be migrated into the lattice of metal NPs and promote atomic diffusion at lower temperature [17]. Therefore, controlled mixing of two atoms is expected by annealing under hydrogen.

2. The miscibility of metals increases with decreasing the size. Therefore, it could be possible that the misciblity drastically increases in sufficiently small NPs.

FeCo is a potential magnetic material because of its high saturation magnetization. It is difficult to control the structure of FeCo in nano-scale. Due to the inhomogeneous mixing, poor crystallinity and oxidation in FeCo NAs the magnetic properties depleted from the bulk material. Therefore, these difficulties should be overcome in order to obtain high saturation magnetization in nano-size. In chapter 2, I aimed to overcome these difficulties by employing hydrogen reduction of PEG stabilized FeCo oxide composite and I studied composition dependent magnetic properties of FeCo NAs.

.

Rh and Cu are immiscible at low temperature according to the phase diagram in bulk state. New properties are expected if RhCu NPs with solid

solution structure are obtained. In chapter 3, I employed co-reduction of two metal ions in aqueous medium in presence of PVP to prepare RhCu NAs. Then, I investigated the catalytic property of the RhCu of different composition NAs for the hydrogenation of 4-nitrobenzaldehyde.

I prepared PVP stabilized Ir NPs and I found that Ir NPs are not simply consists of Ir (0); the NPs are partially oxidized. In chapter 4, I aimed to understand the structure of partially oxidized Ir NPs and I found that small IrO_2 islands are on the surface of Ir NPs. I tested the catalytic activity of this partially oxidized Ir NPs for the hydrogenation of nitroaromatics and compared with other metal NPs (Ir, Pd, Pt, Rh, Au) protected by PVP of comparable size. Ir NPs showed best selectivity among different metals. Finally, I tried to understand the role of oxidized and metallic phase of Ir NPs on the catalysis.

In chapter 5, concluding remarks and the future prospects are given on the basis of the chapters 2-4.

References

1. G. Schmid, in *Nanoparticles: from theory to application*, Wiley-Vch, **2011**.
2. (a) C. Rao, G. Kulkarni, P. J. Thomas, P. P. Edwards, *Chem.-Eur. J.* **2002**, *8*, 28. (b) M. A. El-Sayed, *Acc. Chem. Res.* **2004**, *37*, 326.
3. (a) H. Tsunoyama, H. Sakurai, Y. Negishi, T. Tsukuda, *J. Am. Chem. Soc*. **2005**, *127*, 9374. (b) H. Tsunoyama, H. Sakurai, T. Tsukuda, *Chem. Phys. Lett.* **2006**, *429*, 528.
4. M. J. Hossain, H. Tsunoyama, M. Yamauchi, N. Ichikuni, T. Tsukuda, *Catal. Today* **2012,** *183,* 101.
5. J. N. Kuhn, W. Huang, C.-K. Tsung, Y. Zhang, G. A. Somorjai, *J. Am. Chem. Soc.* **2008**, *130*, 14026.
6. K. M. Bratlie, H. Lee, K. Komvopoulos, P. Yang, G. A. Somorjai, *Nano Lett.* **2007**, *7*, 3097.
7. R. Narayanan, M. A. El-Sayed, *Nano Lett.* **2004**, *4*, 1343.
8. J. Choi, S. J. Oh, H. Ju, J. Cheon, *Nano Lett.* **2005**, *5*, 2179.
9. H. Zhang, T. Watanabe, M. Okumura, M. Haruta, N. Toshima, *Nat. Mater.* **2012**, *11*, 49.
10. N. K. Chaki, H. Tsunoyama, Y. Negishi, H. Sakurai, T. Tsukuda, *J. Phys. Chem. C* **2007**, *111*, 4885.
11. Y. Ito, A. Miyazaki, S. Valiyaveettil, T. Enoki, *J. Phys. Chem. C* **2010**, *114*, 11699.
12. (a) M. Yamauchi, T. Tsukuda, *Dalton Trans.* **2011**, *40*, 4842. (b) J. A. Oyedele, M. F. Collins, *Phys. Rev. B* **1977**, *16*, 3208. (c) M. Nakaya, M.

Kanehara, M. Yamauchi, H. Kitagawa, T. Teranishi, *J. Phys. Chem. C* **2007**, *111*, 7231.

13. N. A. Zarkevich, T. L. Tan, D. D. Johnson, *Phys. Rev. B* **2007**, *75*, 104203.
14. J. Lee, J. C. Park, H. Song, *Adv. Mater.* **2008**, *20*, 1523.
15. J.-I. Park, J. Cheon, *J. Am. Chem. Soc.* **2001**, *123*, 5743.
16. H. Kobayashi, M. Yamauchi, H. Kitagawa, Y. Kubota, K. Kato, M. Takata, *J. Am. Chem. Soc.* **2010**, *132*, 5576.
17. (a) M. Yamauchi, R. Ikeda, H. Kitagawa, M. Takata, *J. Phys. Chem. C* **2008**, *112*, 3294. (b) H. Kobayashi, M. Yamauchi, H. Kitagawa, Y. Kubota, K. Kato, M. Takata, *J. Am. Chem. Soc.* **2008**, *130*, 1828.

Chapter 2

Enhanced Magnetization in Homogeneously Mixed FeCo Nanoalloys

2.1 Introduction

Nanomaterials with high magnetic moments have potential application in various fields, such as data storage, magnetic resonance imaging, and high performance transformers [1]. Nano-scale alloys (nonoalloys; NAs) of Fe-Co are promising materials for these applications because the bulk bcc alloy has the highest saturation magnetization (M_s = 233 emu/g for $Fe_{50}Co_{50}$, 245 emu/g for $Fe_{70}Co_{30}$) [2] in this class of metals and high Curie point (1173 K) [3]. Various synthetic methods of Fe-Co NAs have been proposed, including thermolysis of Fe and Co carbonyl compounds, [4] reduction of Fe^{3+} and Co^{2+} by 1,2-hexadecanediol, [5] reductive thermal conversion of nanometric Prussian blue analogues, [6] polyol method, [7] aqueous reduction method [8] and soft-template method [9]. These methods allow us to control size, [5, 7(b)] morphology, [8(b), 9] and compositions[5, 6, 8(c)]. Despite these efforts, the M_s values of the resulting Fe-Co NAs are still smaller than that of the bulk and fall in the range of 150 – 235 emu/g [4(a), 5, 7(c), 8(c)]. Therefore, the synthesis of Fe-Co NAs displaying the bulk M_s values still remains a challenge. Main reasons for the depletion of the magnetic properties are oxidation in ambient conditions, formation of carbide phase, and poor crystallinity. Post-synthesis thermal treatment can circumvent these problems; this treatment yields bcc Fe-Co NAs covered by a carbon layer for protection against ambient oxidation.

Another structure parameter, which affects the magnetic properties of Fe-Co alloys, is the degree of long range ordering of Fe and Co in bcc structures. It is known that Fe_xCo_{100-x} alloys undergo a transformation between the bcc disordered phase and the B2 (CsCl-type) phase. The B2 phase exists over a range $30 \leq x \leq 70$ [10]. It is reported that the M_s values of the ordered alloys are slightly

larger than those of the disordered alloys both in the bulk and in nano-scale [4(a), 11]. Recently, it is reported that the temperature required for well-ordered alloying can be reduced significantly under hydrogen atmosphere [12]. In addition, well-ordered alloying was achieved during hydrogen adsorption/desorption of a phase-separated, core/shell-type structure [13]. It is also reported that hydrogen can be dissociated and diffused easily on the surface of Fe-Co alloy [14]. These works imply that thermal treatment of Fe-Co NAs under hydrogen enhances the mixing rates of Fe and Co atoms and transforms them into B2 structure, which corresponds to the global minimum structure.

In the present work, I developed a two-step method to prepare solid-solution type, Fe-Co NAs, whose M_s value is as high as bulk alloys, as illustrated in Scheme 1. In the first step (i), small Fe-Co NAs were prepared by rapid and simultaneous reduction of the corresponding metal ions in the presence of stabilizers. The key feature is that individual particles contain both elements with an average composition expected from a molar ratio of the starting compounds. However, the Fe-Co NAs thus prepared were found to be oxidized and phase segregated into Fe_2O_3 and CoO during the workup under ambient condition. In the second step (ii), the oxidized particles were again reduced by heating under hydrogen flow. This treatment induced homogeneous mixing of the two elements and created an amorphous carbon layer, which protect the resulting NAs from oxidation. The evolution of the phase structure was monitored by *in-situ* X-ray diffraction (XRD). Various characterization methods including transmission electron microscopy (TEM), high-resolution TEM (HRTEM), energy-dispersive spectroscopy (EDS) and XRD revealed that Fe-Co NAs prepared by the above method have a solid-solution type and highly crystalline structure. I studied

dependences of particle size and composition on the magnetic properties and found that the $Fe_{70}Co_{30}$ NAs with an average diameter of 30-55 nm showed the M_s value of 250 emu/g, which is the highest in the literature and comparable to that of the bulk alloy (245 emu/g).

2.2 Experimental

2.2.1 Chemicals

Iron (II) acetate ($Fe(OAc)_2$) and Cobalt (II) acetate ($Co(OAc)_2$), poly ethylene glycol (PEG) (M_w: 15000), sodium borohydride ($NaBH_4$), Triethylene glycol (TEG), from Wako Pure Chemical Industries Ltd. were purchased and used without further purification. Deionized water (18 MΩ cm) was used to prepare aqueous solutions.

2.2.2 Preparation

For preparation of a $Fe_{50}Co_{50}$ NA, 1 mmol of $Fe(OAc)_2$ and 1 mmol of $Co(OAc)_2$ were taken in 200 mL of triethylene glycol in presence of 40 mmol polymer (monomeric unit). To dissolve the reactants properly the reaction mixture were put in ultrasonic bath for about 30 min at 25°C. Then argon gas was bubbled into the reaction mixture for 30 min while stirred mechanically. Upon addition of 4 ml aqueous solution of $NaBH_4$ (5M) into the mixed solution at 140 °C, the color of the solution immediately changed from reddish brown into brownish black indicating the formation of Fe–Co NAs (step 1). After cooling the dispersion to room temperature, the black precipitate was obtained by adding 600 ml mixed solvent of acetone and diethyl ether (1:1) and collected by centrifugation. The supernatant was colorless, indicating that the metal precursor

ions were completely reduced to form the precipitates. The precipitates were oxidized under ambient conditions and gave phase segregated oxide composites, composed of Fe_2O_3 and CoO. The oxide composites were reduced again by heating under hydrogen flow (step 2) with thermogravimetry (TG) instrument (Bruker, MTC1000SA) by flowing hydrogen at 200 mL/min at 450 °C. Monometallic Fe and Co NPs were also prepared as references in a similar manner.

Scheme 2.1. Preparation procedure of Fe-Co NAs by the two-step reduction.

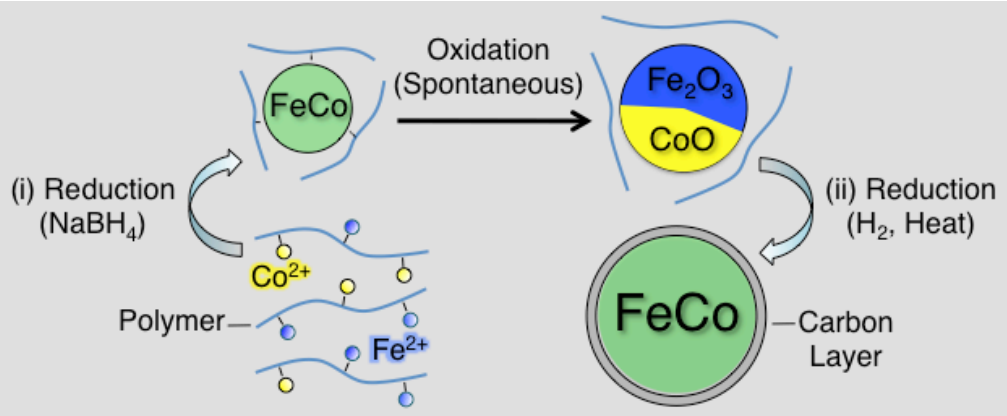

2.2.3 Characterization

A. Transmission electron microscopy (TEM)

A drop of NAs dispersion (~0.4 mM) in ethanol was put on a hydrophobic film coated TEM grid and the solvent was dried naturally. Transmission Electron Microscope (JEM-2100F, JEOL) operated at 200 kV was used to study the morphology and the average size at different magnification ranging from 100,000–250,000.

B. Powder X-ray diffraction (XRD)

The finely powdered samples were put on a glass holder and slightly pressed with a glass slide to flatten the samples. Powder X-ray diffraction (XRD) profiles of the solid samples of NAs were measured by using a D8 Advance diffractometer (Bruker) with a radiation source of Cu Ka (1.5418 Å) operated at 40 kV and 40 mA.

C. *In situ* X-ray diffraction (XRD)

In situ XRD was carried out using synchrotron radiation at the BL44B2 of the SPring-8 the X-ray having wavelength of 0.579088(3) Å. The diffraction patterns of samples in a glass capillary were taken under controlled hydrogen atmosphere (0–0.1 MPa). Rietveld analysis was performed by using Topas4 fitting software.

D. Elemental mapping

High-angle annular dark-field scanning TEM (HAADF- STEM) and scanning TEM EDS (STEM-EDS) mappings were recorded with a JEM-ARM200F (JEOL) operated at 200 kV.

E. Magnetic measurements

M-H magnetization curves were measured for the NAs and monometallic Fe and Co using the MPMS XL superconducting interference device magnetometer (Quantum Design) in the field range of `20 kOe at 300 K.

F. Inductively coupled plasma atomic emission spectroscopy (ICP-AES)

The metal content and composition of the FeCo NAs were determined by using an inductively coupled plasma atomic emission spectrometer (ICPE-9000, Shimadzu). Approximately 3-10 ppm concentration of samples were prepared by

dissolving solid FeCo NAs in 8 % (volume) aqua regia. A series of standard solution (1-10 ppm) of Fe and Co were used to calibrate the spectrophotometer.

2.3 Results and Discussion

Figure 2.1a shows a typical TEM image of the PEG stabilized oxide composite obtained from the reaction solution of Fe:Co = 50:50. The composite is composed of small grains of about 5 nm in diameter. Powder XRD pattern of the oxide composite was reproduced by a superposition of diffraction patterns of Fe_2O_3 and CoO nanocrystallites with the size of 2.5 and 2.9 nm, respectively (Figure 2.1b). The above results indicate that FeCo NAs once formed by co-reduction were oxidized into phase-segregated oxide particles during the workup under the ambient condition. I hereafter refer to the samples (oxide composites) as $Fe_xCo_{100-x}O_y$/PEG or $Fe_xCo_{100-x}O_y$/PVP, where x represents the relative atomic ratio of Fe as compared to the total number of metal atoms used in the above preparation (Scheme 2.1).

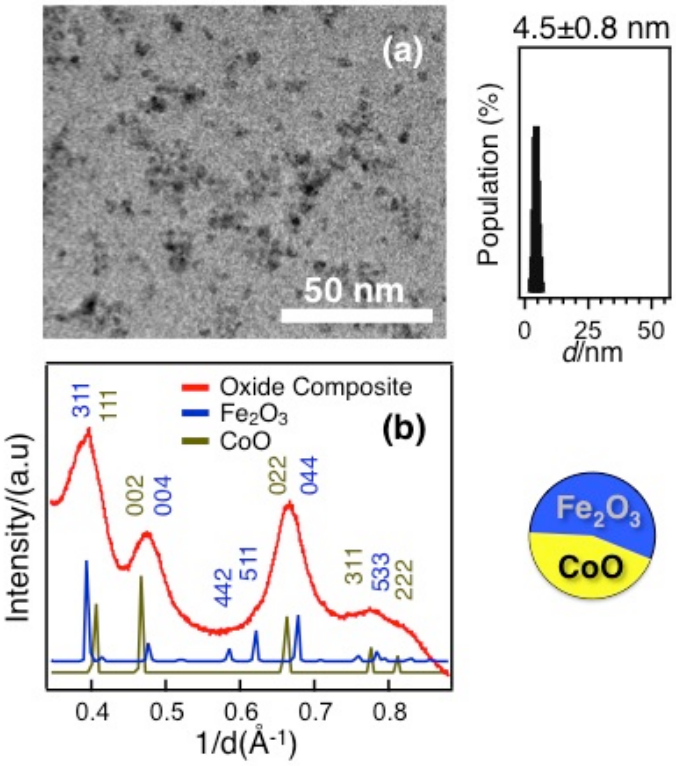

Figure 2.1. (a) TEM image and (b) XRD pattern of $Fe_{50}Co_{50}O_y$/PEG composite.

The $Fe_xCo_{100-x}O_y$/PEG composites were then heated at 450 °C under hydrogen (0.1 MPa) for 0.5 h (step ii). Here, details of the structure analysis are given for the calcined sample of $Fe_{50}Co_{50}O_y$/PEG as an example. Figure 2.2a shows the typical TEM image of $Fe_{50}Co_{50}$. The average size of the particles was 30 ± 5 nm. The HRTEM image of $Fe_{50}Co_{50}$ (Figure 2.2b) demonstrates that the particle is highly crystalline with periodic lattice fringes. The lattice spacing of 0.20 nm corresponds to the distance between (011) planes of bcc $Fe_{50}Co_{50}$ alloy (0.202 nm). Close inspection of the HRTEM image suggests a formation of amorphous carbon layer on the surface. The carbon layer was formed from the stabilizing polymer of the metal oxide composite by the heat treatment. The powder XRD pattern (Figure 2.2c) could be fitted by assuming single-phase bcc

type structure, in which Fe and Co forms a solid solution type alloy. I did not observe XRD patterns of the oxide phases for the calcined samples even though they were measured after storage for 3 months under ambient conditions. Thus, the calcined samples are referred to as Fe_xCo_{100-x}. The crystalline size calculated by Scherrer analysis of the XRD pattern of $Fe_{50}Co_{50}$ (Figure 2.2c) was 32 nm, which is consistent with the size estimated from TEM.

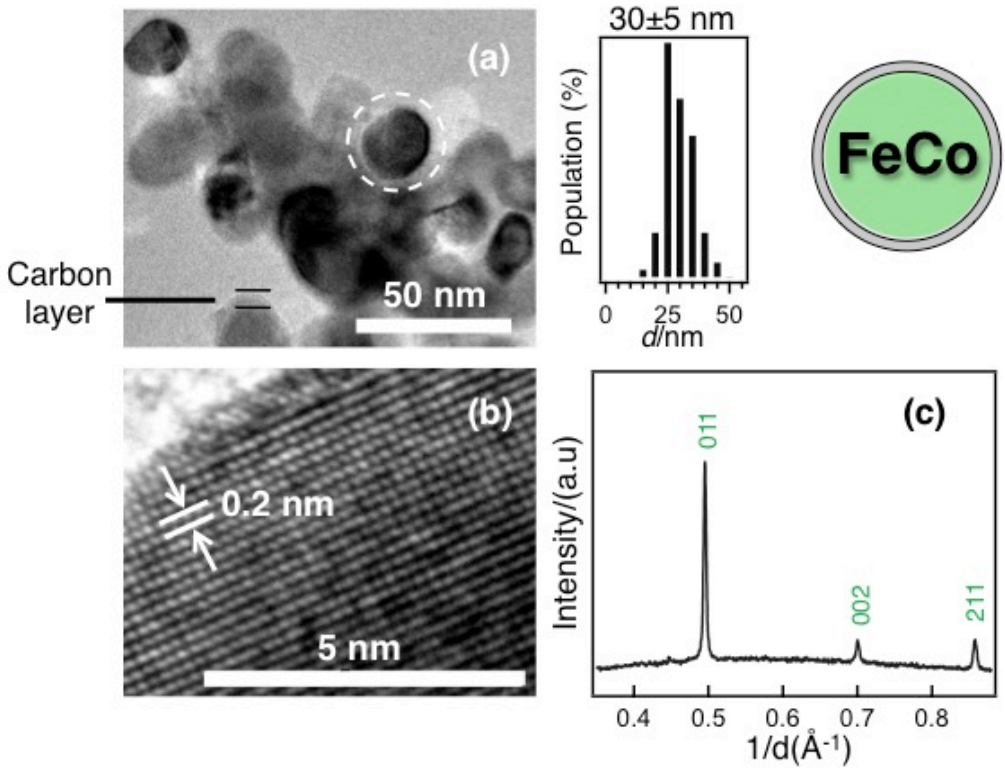

Figure 2.2. (a) TEM image of $Fe_{50}Co_{50}$ NAs prepared from $Fe_{50}Co_{50}O_y$/PEG. (b) HRTEM image of a section of a single particle circled in (a). (d) Powder XRD pattern of the $Fe_{50}Co_{50}$ NAs prepared from $Fe_{50}Co_{50}O_y$/PEG.

Figure 2.3a shows a HAADF-STEM image of $Fe_{50}Co_{50}$ NAs calcined under hydrogen. Figure 2.3b and 2.3c show the STEM-EDS elemental maps for Fe and Co, respectively. Both constituent atoms in the $Fe_{50}Co_{50}$ NAs are homogeneously distributed, which gives the evidence of formation of solid-

solution alloy.

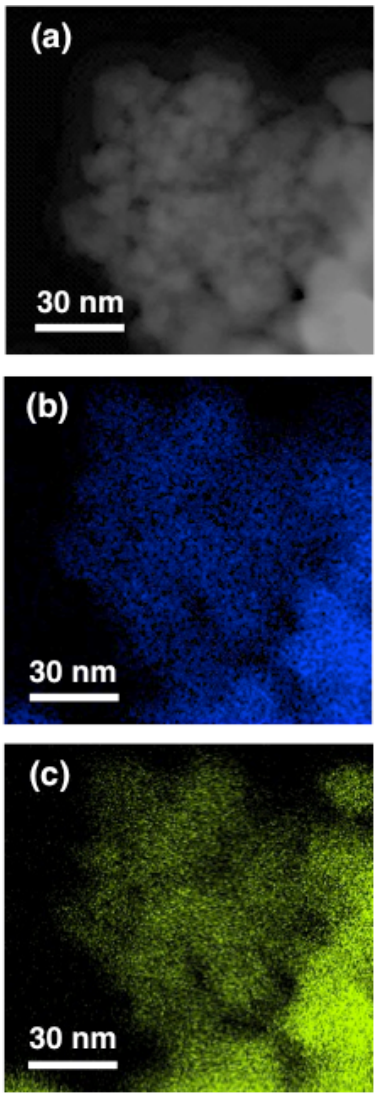

Figure 2.3. (a) HAADF-STEM image, (b) Fe-K and (c) Co-K STEM-EDS maps of $Fe_{50}Co_{50}$ NAs.

The effect of hydrogen atmosphere on structural changes during heating was studied by *in-situ* XRD measurement. Figure 2.4 shows the XRD patterns of $Fe_{50}Co_{50}O_y$/PEG with and without hydrogen while changing the temperature. The XRD patterns were analyzed by Rietveld method by assuming four phases; $Fe_{50}Co_{50}$ alloy with bcc structure, iron oxides (Fe_2O_3, FeO) and cobalt oxide (CoO). The formation of FeO phase suggests that reduction of Fe_2O_3 by H_2

proceeds via the FeO phase. The relative populations of the four phases in $Fe_{50}Co_{50}$ alloy are plotted as a function of temperature under hydrogen and vacuum in Figure 2.5a and 2.5b, respectively. Under hydrogen atmosphere, the $Fe_{50}Co_{50}$ alloy phase appeared at 350°C and its population monotonically increased with temperature while those of Fe_2O_3/FeO and CoO phases decreased with a similar rate (Figure 2.5a). This behavior indicates that $Fe_{50}Co_{50}$ alloy phase is formed through the simultaneous reduction of Fe_2O_3/FeO and CoO phases. On the other hand, the alloy phase was not formed even at 500 °C under vacuum. Only a half of CoO phase was reduced to Co phase, whereas Fe_2O_3/FeO was not reduced at all. This indicates that hydrogen plays an essential role for the simultaneous reduction of both oxide phases as well as for homogeneous mixing of constituent atoms to form solid solution Fe-Co alloy.

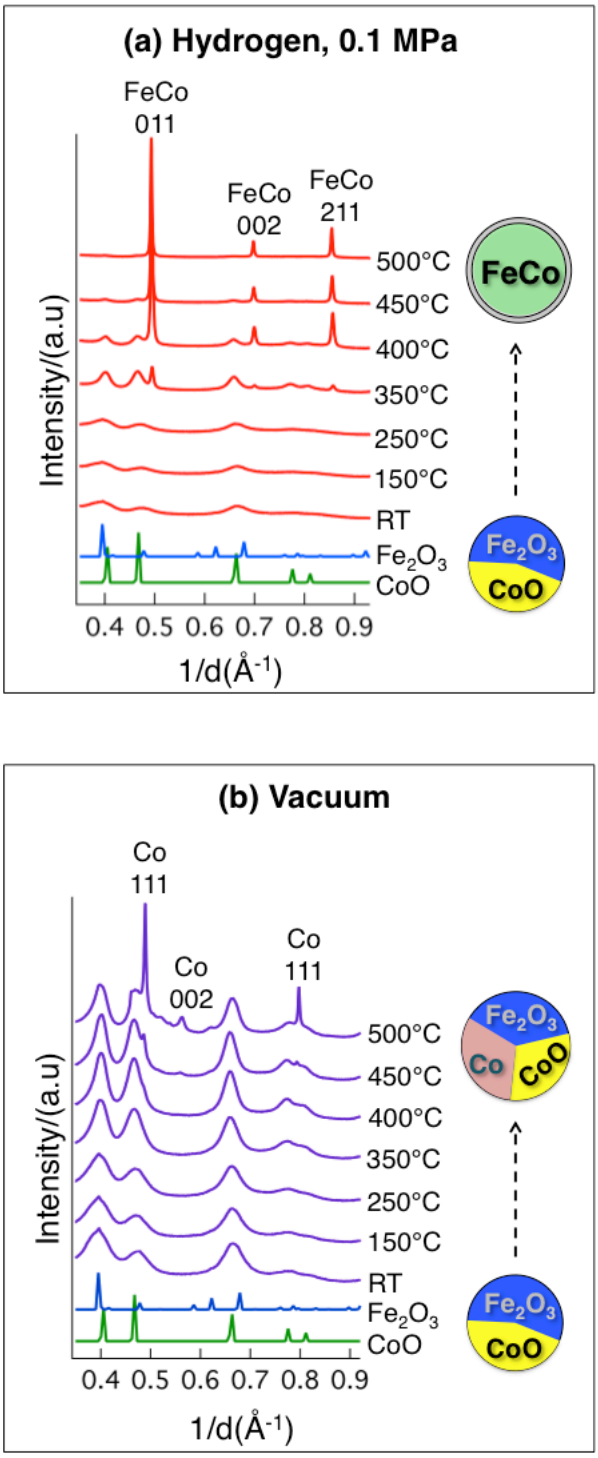

Figure 2.4. *In-situ* XRD patterns of $Fe_{50}Co_{50}O_y$/PEG during heating under (a) 0.1 MPa hydrogen and (b) vacuum. XRD patterns of Fe_2O_3 and CoO are indicated at the bottoms.

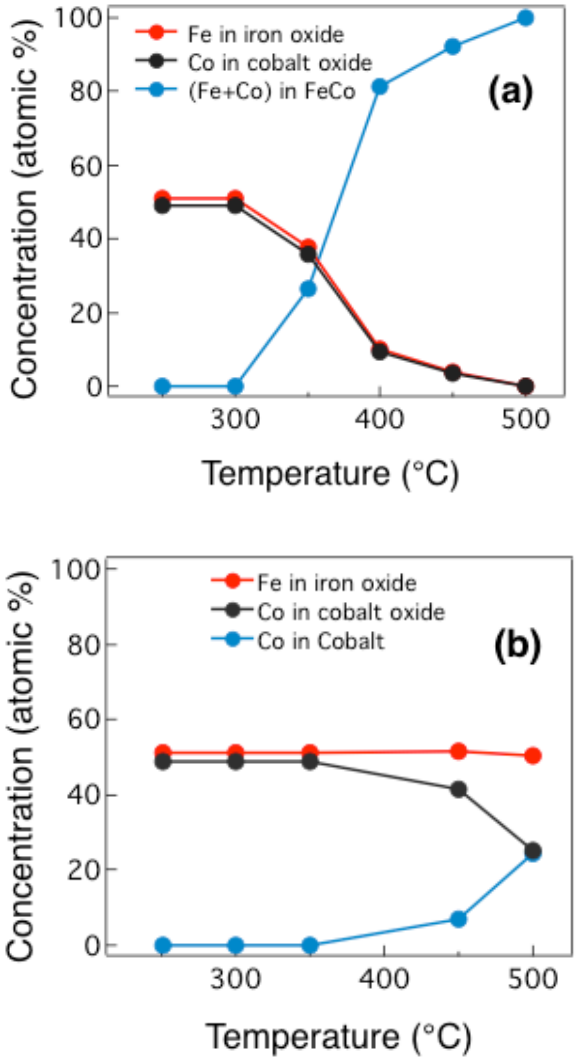

Figure 2.5. Phase populations in $Fe_{50}Co_{50}O_y$/PEG as a function of temperature under (a) 0.1 MPa hydrogen and (b) vacuum.

In order to reveal the effect of the compositions on the magnetic properties, it is required to prepare NAs with various compositions while keeping the diameters constant. However, this is a technical challenge at the present stage. As an initial step towards such goal, I prepared Fe_xCo_{100-x} ($20 \leq x \leq 80$) NAs in the size range of 30-55 nm. The atomic ratios of Fe and Co in the NAs were proportional to those of precursor metals used in the synthesis (Figure 2.6). Powder XRD patterns indicated that Fe_xCo_{100-x} NAs are composed of a pure Fe-Co alloy phase

(Figure 2.7) except for $Fe_{20}Co_{80}$ in which fcc Co phase is additionally observed. The distance between (111) planes increases with increasing Fe ratio. The average size estimated from XRD and TEM (Figure 2.8) are consistent and in the range of 30–45 nm (table 2.1).

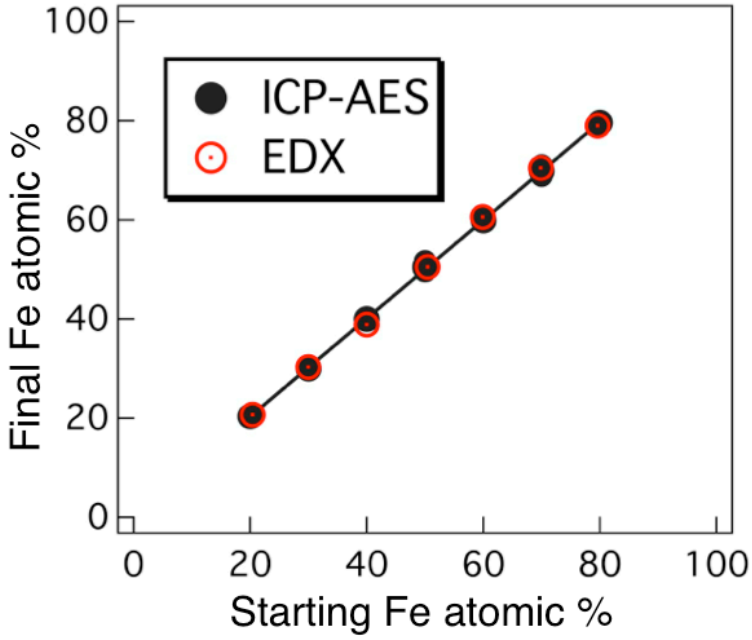

Figure 2.6. Linearity between starting and final compositions of Fe_xCo_{100-x} NAs.

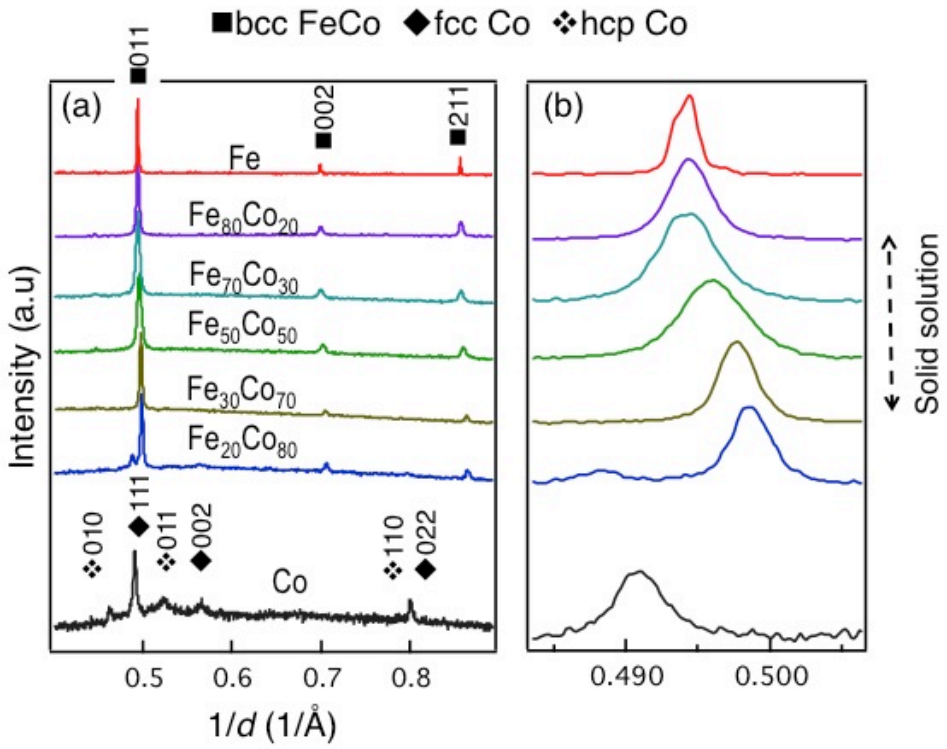

Figure 2.7. (a) XRD patterns of Fe_xCo_{100-x} NAs and (b) its expanded view at 011 position.

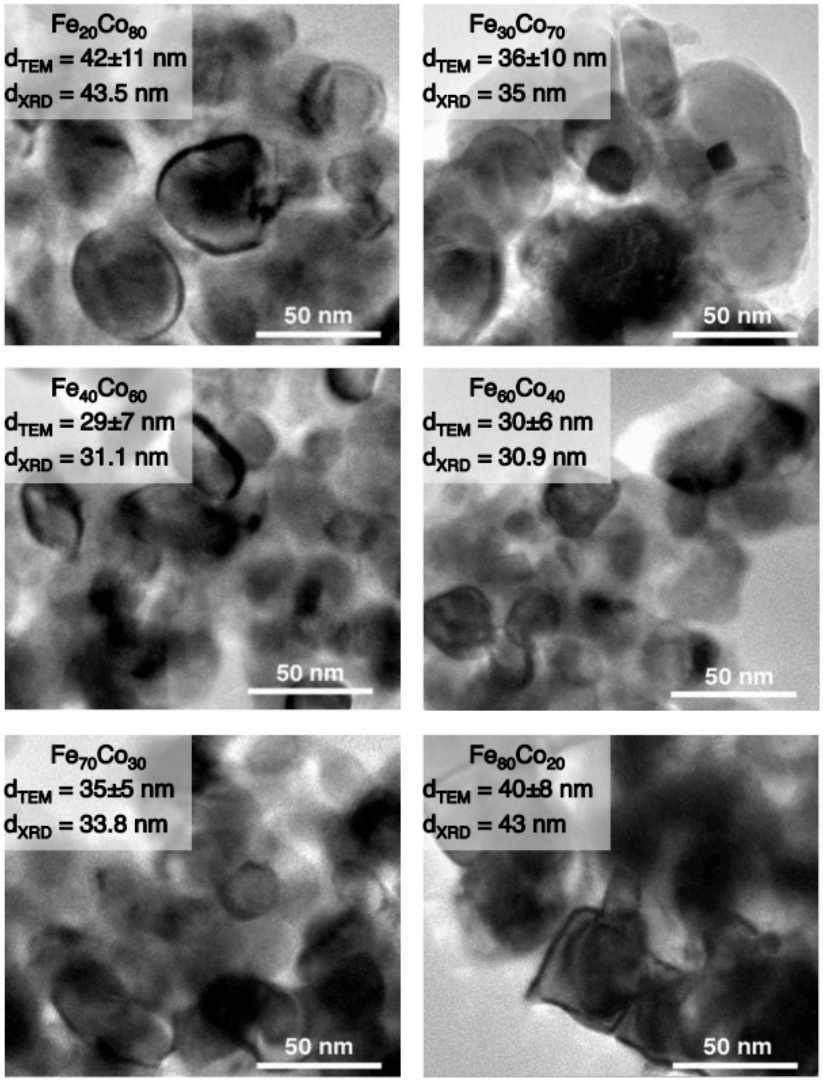

Figure 2.8. TEM images of Fe_xCo_{100-x} NAs.

Table 2.1. Diameters of Fe_xCo_{100-x} NPs determined by TEM and XRD analyses.

Sample	Diameter	
	d_{TEM} (nm)	d_{XRD} (nm)
$Fe_{20}Co_{80}$	42 ± 11	44
$Fe_{30}Co_{70}$	36 ± 10	35
$Fe_{40}Co_{60}$	29 ± 7	31
$Fe_{50}Co_{50}$	30 ± 5	32
$Fe_{60}Co_{40}$	30 ± 6	31
$Fe_{70}Co_{30}$	35 ± 5	34
$Fe_{80}Co_{20}$	40 ± 8	43

Figure 2.9a shows the magnetization curves for $Fe_{50}Co_{50}$ NAs and monometallic Fe, Co NPs. The magnetization was normalized by the total weight of the metals determined by ICP-AES analysis. The $Fe_{50}Co_{50}$ NAs exhibited ferromagnetic behavior with a typical hysteresis loop and a larger M_s value compared to the monometallic NPs.

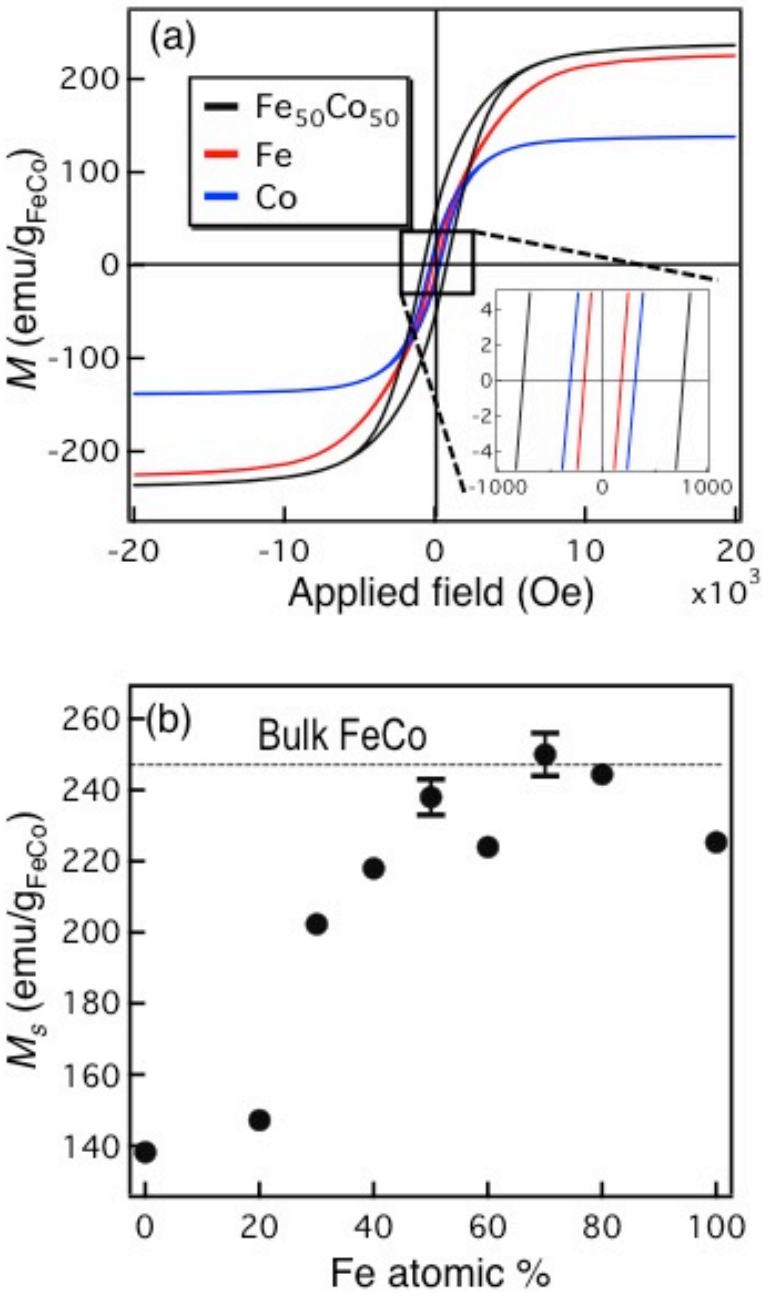

Figure 2.9. (a) Magnetization curves for $Fe_{50}Co_{50}$ NAs and Fe, Co NPs at 300 K. (b) Composition dependency on M_s of Fe_xCo_{100-x} NAs.

The magnetization behavior depended strongly on the composition. The M_s values were plotted as a function of the composition in Figure 2.9b. The FeCo NAs synthesized in this study showed very high M_s values. The average M_s values of $Fe_{50}Co_{50}$ and $Fe_{70}Co_{30}$ NAs were determined to be 238±5 and 250±6

emu/g, respectively, from the three batches of the samples (Figure 2.9b). It is notable that these values are comparable to those of corresponding bulk alloy (233 emu/g for $Fe_{50}Co_{50}$ and 245 emu/g for $Fe_{70}Co_{30}$) [2]. TEM, XRD and elemental mapping results suggested that constituent metals in the Fe-Co are homogeneously mixed. It is, therefore, supposed that homogeneous mixing of constituent metals promotes electronic interactions among metals, resulting in a large M_s values as observed in the ordered Fe-Co alloys.

2.4 Summary

In conclusion, I prepared homogeneously mixed, solid-solution Fe-Co NAs by hydrogen reduction of the mixed oxide composites. The M_s values of Fe-Co alloys with 30-55 nm in diameter are higher than those reported previously and comparable to that of corresponding bulk Fe-Co alloys. The heat treatment under hydrogen is found to be feasible for improving crystallinity and for promoting electronic interaction of constituent elements similarly to those achieved in the ordered Fe-Co alloy systems, which gives the largest M_s.

References

1. S. Sugimoto, *J. Phys. D: Appl. Phys.* **2011**, *44*, 064001.
2. Weiss, P. *Trans. Faraday Soc.* **1912**, *8*, 149.
3. C. Jo, J. Lee, Y. Jang, *Chem. Mater*. **2005**, *17*, 2667.
4. (a) C. Desvaux, C. Amiens, P. Fejes, P. M. Respaud, P. Lecante, E. Snoeck, B. Chaudret, *Nat. Mater.* **2005**, *4*, 750. (b) V. Tzitzios, G. Basina, D. Niarchos, W. Li, G. V. Hadjipanayis, *J. Appl. Phys.* **2011,** *109*, 07A313-1.
5. G. S. Chauvey, C. Barcena, N. Poudyal, C. Rong, J. Gao, S. Sun, J. P. Liu, *J. Am. Chem. Soc.* **2007**, *129*, 7214.
6. M. Yamada, S. Okumura, K. Takahashi, *J. Phys. Chem. Lett.* **2010,** *1*, 2042.
7. (a) D. Kodama, K. Shinoda, K. Sato, Y. Sato, B. Jeyadevan, K. Tohji, *IEEE Trans. Magn.* **2006**, *42*, 2796. (b) D. Kodama, K. Shinoda, K. Sato, Y. Sato, B. Jeyadevan, K. Tohji, *J. Mag. Mag. Mater.* **2007**, *310*, 2396. (c) Z. J. Huba, K. J. Carroll, E. E. Carpenter, *J. Appl. Phys.* **2011**, *109*, 07B514-1. (d) M. Zamanpour, Y. Chen, B. Hu, K. Carroll, Z. J. Huba, E. E. Carpenter, L. H. Lewis, V. G. Harris, *J. Appl. Phys.* **2012**, *111*, 07B528-1.
8. (a) C. W. Kim, Y. H. Kim, H. G. Cha, H. W. Kwon, Y. S. Kang, *J. Phys. Chem. B* **2006**, *110*, 24418. (b) X. W. Wei, G. X. Zhu, Y. J. Liu, Y. H. Ni, Y. Song, Z. Xu, *Chem. Mater.* **2008**, *20*, 6248. (c) K. J. Carroll, D. M. Hudgins, L. W. Brown III, S. D. Yoon, D. Heiman, V. G. Harris, E. E. Carpenter, *J. Appl. Phys.* **2010,** *107*, 09A303-1.
9. S. K. Pal, D. Bahadur, *Mater. Lett.* **2010**, *64*, 1127.

10. J. A. Oyedele, M. F. Collins, *Phys. Rev. B* **1977**, *16*, 3208.

11. A. Díaz-Ortiz, R. Drautz, M. Fähnle, H. Dosch, J. M. Sanchez, *Phys. Rev. B* **2006**, **73**, 224208-1.

12. (a) M. Yamauchi, T. Tsukuda, *Dalton Trans.* **2011**, *40*, 4842, (b) M. Okada, A. Kamegawa, J. Nakahigashi, A. Yamaguchi, A. Fujita, M. Yamauchi, *Mater*. *Sci*. *Eng*. **2010**, 173, 253. (c) M. Yamauchi, R. Abe, T. Tsukuda, K. Kato, M. Takata, *J*. *Am*. *Chem*. *Soc*. **2011**, *133*, 1150.

13. H. Kobayashi, M. Yamauchi, H. Kitagawa, Y. Kubota, K. Kato, M. Takata, *J. Am. Chem. Soc.* **2010,** *132*, 5576.

14. J. M. H. Lo, T. Ziegler, *J. Phys. Chem. C* **2008**, *112*, 3667.

Chapter 3

Selective Hydrogenation of Nitroaromatics by Homogeneously Mixed RhCu Nanoalloys

3.1 Introduction

Bimetallic NPs often show improved properties than monometallic NPs by the modification of electronic structures of NPs [1]. The degree of modification of the electronic structures is greatly enhanced in solid solution structures rather than in a phase separated or core-shell structures [2]. Therefore, productions of solid solution structures are required in order to explore new properties of catalysis, magnetism, and so on. However, it is considered that bimetallic NPs with solid solution structures are produced only with a limited number of combinations according to phase diagram in bulk state.

Several theoretical papers suggest that phase diagram in the bulk and that in nano scale are different due to difference in surface energy, melting point, transition temperature, solubility etc. [3]. Recently, few experimental reports demonstrated the formation of NAs with solid solution structures of two metals, which are immiscible in bulk state. Kusada *et al.* reported the solid solution alloy of Rh-Ag by a ethylene glycol reduction method [4]. Essinger-Hileman *et al.* reported the formation of Au-Rh, Au-Pt, Pt-Rh, Pd-Rh NAs with average diameter of 10 nm by a chemical reduction method [5].

Rh and Cu are also immiscible in the bulk state at low temperature according to the phase diagram as shown in Figure 3.1. At a high temperature (~1000 °C), there exist several meta-stable solid solution structures, which undergo phase separation into pure phases composed of Rh and Cu at lower temperature [6]. Several theoretical reports also predicted the phase separation of Rh-Cu due to positive enthalpy of formation between Rh and Cu [7]. In this study, I discovered the formation of a solid solution structure in NPs (~2.5 nm) formed by rapid reduction of the two metal ions in aqueous medium in the

presence of poly(*N*-vinyl-2-pyrrolidone) (PVP) as a stabilizer.

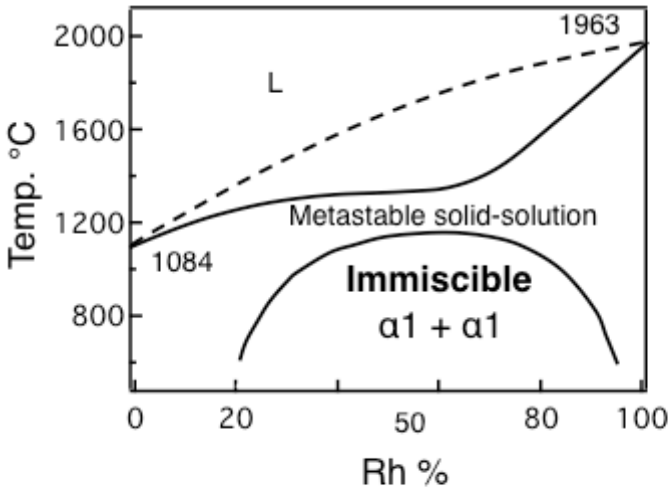

Figure 3.1. Phase diagram of Rh-Cu system in bulk state.

Nakamura *et al.* demonstrated that dendrimer stabilized RhFe NAs can hydrogenate nitroarenes and olefins at room temperature and atmospheric hydrogen pressure [8]. Although the selectivity issue has not been studied in this case, this report suggests that bimetallic NAs of Rh is a potential candidate for the selective hydrogenation of nitroaromatics. The catalytic property of the prepared RhCu NAs has been tested for the hydrogenation of nitrobenzaldehyde.

3.2 Experimental

3.2.1 Chemicals

Rhodium (III) acetate from Mitsuwa Pure Chemical Industries Ltd; Copper (II) sulfate (CuSO4) sodium borohydride ($NaBH_4$), PVP (M_w: 40 kDa) from Wako Pure Chemical Industries Ltd; were purchased and used without further purification. Deionized water (18 MΩ cm) was used to prepare aqueous solutions.

3.2.2 Preparation

Scheme 1 shows the general preparation procedures for RhCu NAs. For the preparation of a $Rh_{50}Cu_{50}$ NA, 0.075 mmol of $Rh(OAc)_3$ and 0.075 mmol of $CuSO_4$ were taken in 50 mL of deionized water in presence of 3.0 mmol (in a monomer unit) of PVP (K30, MW = 40 kDa). Then argon gas was bubbled into the reaction mixture for 30 min while stirred magnetically. Upon addition of 5 mL of aqueous solution of $NaBH_4$ (20 eq. with respect to the metal) to precursor solution at 25 °C the color of the solution immediately changed into dark black which indicates the formation of NPs. The reaction system was kept in vigorous stirring for another 30 min. After 30 min, the colloidal dispersion of the NAs were collected by passing through a membrane filter having molecular cut-off of 10 kDa to remove any inorganic moieties. The collected dispersion were further washed with deionized water and dried in lyophilizer. In the similar procedure, monometallic Rh NPs and the other composition of the RhCu NAs were prepared.

Scheme 3.1 Preparation scheme for the RhCu NAs.

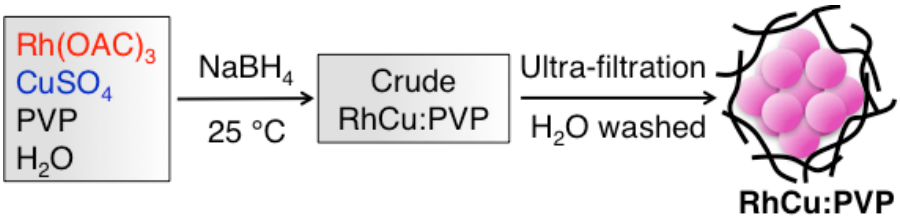

3.2.3 Characterization

A. UV-Visible spectroscopy

UV-visible spectra of RhCu:PVP dispersed in water were recorded by using a spectrophotometer (V-670, JASCO) under ambient condition.

B. Transmission electron microscopy (TEM)

A drop of RhCu:PVP dispersion (~0.4 mM) in ethanol was put on a hydrophobic film coated TEM grid and the solvent was dried naturally. Transmission Electron Microscope (HF-2000F, Hitachi) operated at 200 kV was used to study the morphology and the average size at different magnification ranging from 100,000–250,000.

C. Powder X-ray diffraction (XRD)

The finely powdered samples were put on a glass holder and slightly pressed with a glass slide to flatten the samples. Powder X-ray diffraction (XRD) profiles of the solid samples of RhCu:PVP were measured by using a diffractometer (Miniflex, Rigaku) with a radiation source of Cu Ka (1.5418 Å) operated at 30 kV and 15 mA.

3.2.4 General Procedure for Catalytic Hydrogenation

Hydrogenation reactions were carried out in a Teflon tube reactor settled inside a stainless steel autoclave. For a typical reaction, the ethylacetate solution of nitrobenzaldehyde (0.4 M, 1 mL) was added to the hydrosol (4 mL) of RhCu:PVP containing 8 μmol of metal atoms. The autoclave were flushed with H_2 for 5 times and finally pressurized with 0.1 MPa of H_2. The biphasic system was then vigorously stirred at 25 °C under hydrogen (0.1 MPa). After 2 h, the organic layer was separated, and the products were analyzed by gas

chromatography and gas chromatography–mass spectrometry.

3.3 Results and Discussion

Figure 3.2 shows UV-Vis spectra of the RhCu:PVP NAs along with the pure Rh:PVP NPs. These spectra showed a exponential decay profile toward longer wavelength, which is typical for metal NPs. The well-known plasmon peak for Cu NPs around 566 nm was absent [9]. The absence of the plasmon peak suggests that Cu atoms are homogeneously mixed within the lattice of Rh to form solid-solution structure rather than forming a separated domain of Cu and Rh NPs.

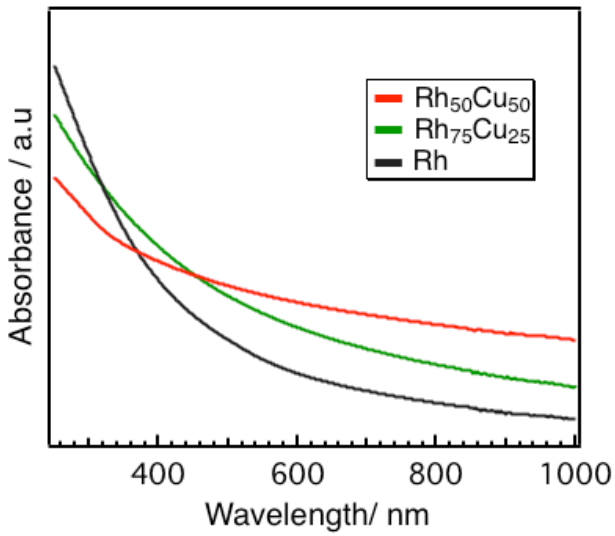

Figure 3.2. UV-Vis spectra of colloidal dispersion of RhCu NAs and Rh NPs.

Representative TEM images of the RhCu:PVP and Rh:PVP are shown in Figure 3.3. The average sizes were estimated from measuring the diameters of more than 200 particles to be 2.5±0.5 and 2.6±0.6 nm for $Rh_{75}Cu_{25}$ and $Rh_{50}Cu_{50}$, respectively, which were slightly larger than monometallic Rh:PVP. The structures of these NAs were confirmed Powder XRD patterns (Figure 3.4). The XRD patterns of $Rh_{75}Cu_{25}$ and $Rh_{50}Cu_{50}$ showed face centered cubic (fcc) single-

phase type structure. The peak position at 111 planes shifted to higher angle with increasing Cu content. NAs having Cu content more than 50 % ($Rh_{40}Cu_{60}$) have a phase-separated structure having an additional phase of Cu_2O. The crystalline sizes estimated from the Scherrer equation were 2.3 nm for both $Rh_{75}Cu_{25}$ and $Rh_{50}Cu_{50}$ NAs, which are in good agreement with the TEM results.

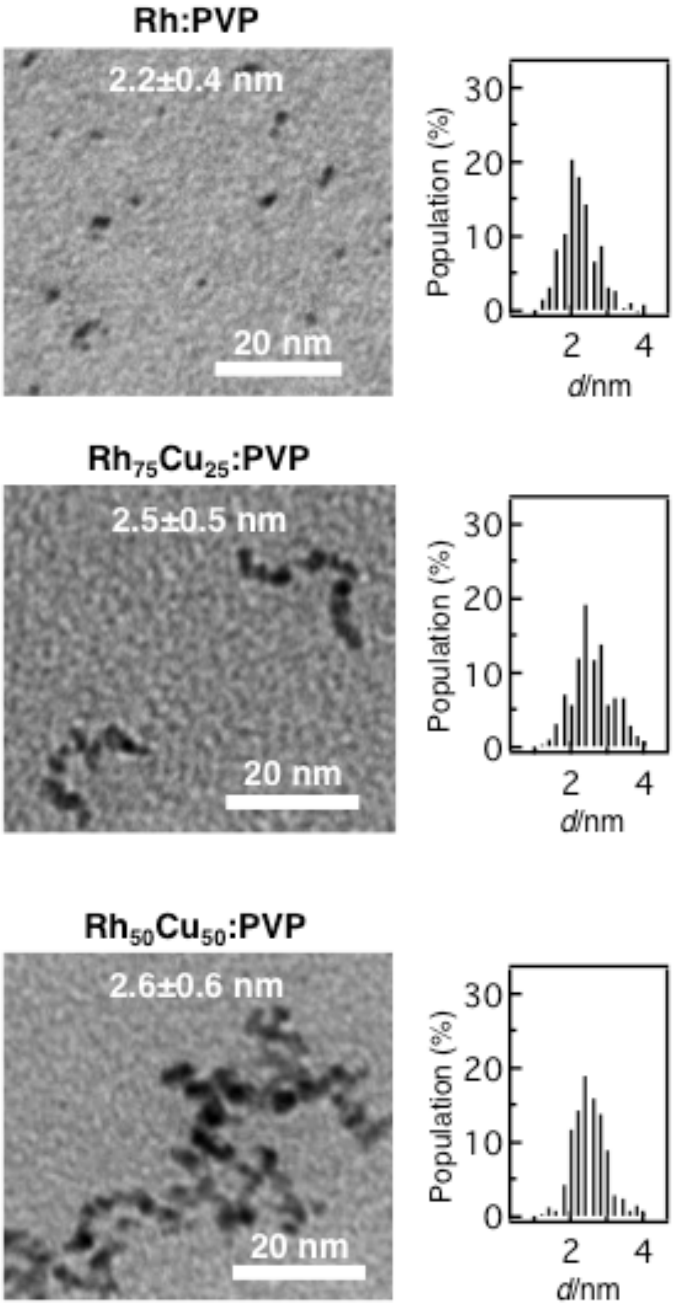

Figure 3.3. TEM images of RhCu NAs and Rh NPs.

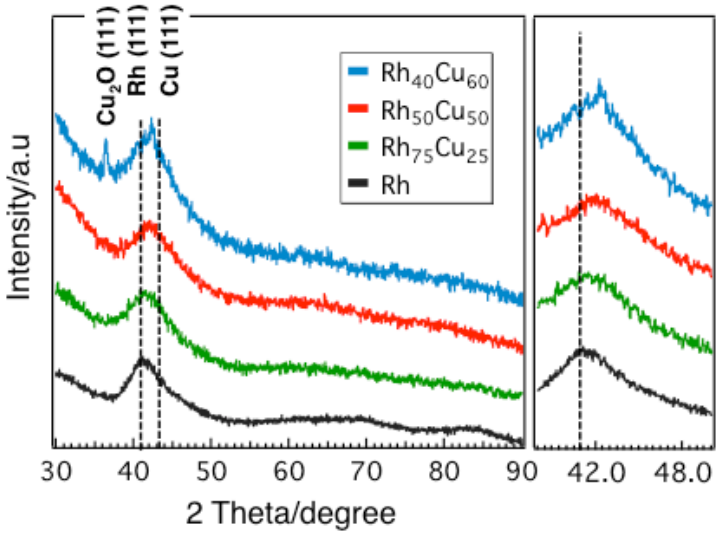

Figure 3.4. XRD patterns of RhCu NAs and Rh NPs (left) and the expanded view around 111 position (right).

The lattice constants of the NAs were calculated from the corresponding d_{111} (distances between 111 plane) values according to equation (1) [10].

$$1/d^2 = (h^2 + k^2 + l^2)/a^2 \quad \ldots\ldots\ldots\ldots\ldots\ldots (3.1)$$

d = lattice spacing, a = lattice constant

λ = wavelength of radiation (1.542 Å)

Table 3.1 summarizes the structural parameters for these NAs. The lattices constants were found to increase with increasing Rh content and scale linearly with the composition of the NAs (Figure 3.5) following the Vegard's law, which states a liner relationship of lattice constants with the composition for the solid solution structure [11]. This behavior in the lattice constants reveals that the structures of $Rh_{75}Cu_{25}$ and $Rh_{50}Cu_{50}$ are solid solution.

Table 3.1 Structural characterizations of RhCu NAs

Composition	d_{TEM} (nm)	d_{XRD} (nm)	a / Å
$Rh_{100}Cu_0$	2.2	2.0	3.787
$Rh_{75}Cu_{25}$	2.5	2.3	3.759
$Rh_{50}Cu_{50}$	2.6	2.3	3.726

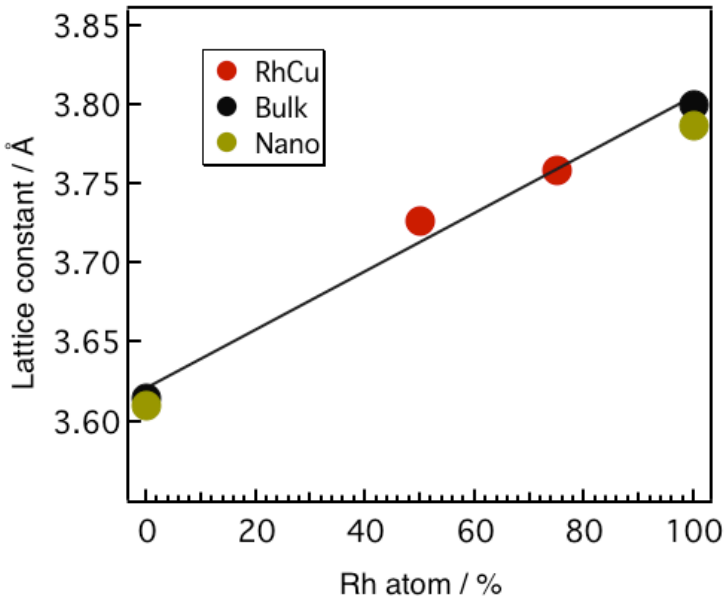

Figure 3.5. Composition dependency on lattice constants of RhCu NAs.

The origin of the formation of solid solution structure in nano-size can be explained in terms of size dependent solubility according to the previous reports. It has been reported that the solubility of tin (Sn) in lead (Pb) increases with the reduction of size [3d, 12]. The surface energy of a small NP is very high as compared to that in the bulk. This high surface energy increased the overall chemical potential (Gibbs energy), which can enhance the heterometallic atomic diffusion [12].

The catalytic performance of RhCu:PVP was tested and compared with Rh NPs using hydrogenation of 4-nitrobenzaldehyde (**1**) as a test reaction. The results of the catalytic tests are summarized in Figure 3.6. In all cases, partially

reduced species, 4-aminobenzaldehyde (**2**), and fully reduced species, 4-aminobenzyl alcohol (**3**), were obtained as the products. 4-Nitrobenzyl alcohol was not produced. Conversions of **1** under these mild conditions were nearly 100 %. However, selectivity towards **2** was strongly dependent on the composition the NAs: $Rh_{50}Cu_{50}$ NAs showed the highest selectivity.

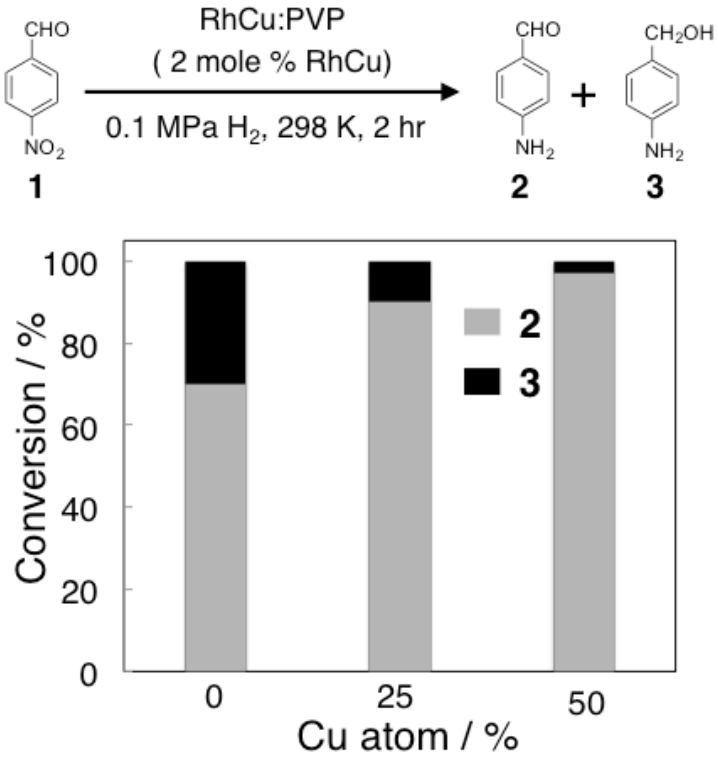

Figure 3.6. Composition dependency of RhCu on hydrogenation of 4-nitrobenzaldehyde.

Finally I speculate the possible reason for the high selectivity by $Rh_{50}Cu_{50}$ - which is based on the electronic transfer from Cu to Rh [13]. Such an electronic transfer can create slight negative charge on Rh and slight positive charge on Cu. On the other hand NO_2 group of nitrobenzaldehyde carried an ionic charge having positively charged nitrogen and negatively charged oxygen. Such a $Rh^{\delta-}$ $Cu^{\delta+}$ surface composition is suitable for the preferential adsorption of the NO_2 group of the nitroaromatic molecule because of the positive charge on nitrogen

and negative charge on oxygen of NO_2 group. Therefore, NO_2 group is selectively adsorbed and reduced to NH_2 group.

3.4 Summary

In summary, I have discovered the solid solution structure of the RhCu bimetallic alloy in nano-size. The latttice constants value of the the NAs follow the Vegars`s law which clearly reavealed that the structures are solid solution. These NAs acted as active catalyst for the hydrogenation of nitrobenzaldehyde under mild conditions (298 K and 0.1 MPa of H_2).

References

1. (a) J. R. Kitchin, J. K. Norskov, M. A. Barteau, J. G. Chen, *J. Chem. Phys.* **2004**, *120*, 10240. (b) N. K. Chaki, H. Tsunoyama, Y. Negishi, H. Sakurai, T. Tsukuda, *J. Phys. Chem. C* **2007**, *111*, 4885. (c) H. Zhang, T. Watanabe, M. Okumura, M. Haruta, N. Toshima, *Nat. Mater.* **2012**, *11*, 49. (d) C. M. Andolina, A. C. Dewar, A. M. Smith, L. E. Marbella, M. J. Hartmann, J. E. Millstone, *J. Am. Chem. Soc.* **2013**, *135*, 5266.
2. (a) H. Kobayashi, M. Yamauchi, H. Kitagawa, Y. Kubota, K. Kato, M. Takata, *J. Am. Chem. Soc.* **2010**, *132*, 5576. (b) J.-I. Park, J. Cheon, *J. Am. Chem. Soc.* **2001**, *123*, 5743.
3. (a) M. Wautelet, J. P. Dauchot, M. Hecq, *Nanotechnology* **2000**, *11*, 6. (b) J. G. Lee, H. Mori, H. Yasuda, *Phys. Rev. B* **2002**, *65*, 132106. (c) A. S. Shirinyan, M. Wautelet, *Nanotechnology* **2004**, *15*, 1720. (d) A. S. Shirinyan, A. M. Gusak, M. Wautelet, *Acta Materialia* **2005**, *53*, 5025. (e) G. Manai, F. Delogu, *Physica B: Condensed Matter* **2007**, *392*, 288.
4. K. Kusada, M. Yamauchi, H. Kobayashi, H. Kitagawa, Y. Kubota, *J. Am. Chem. Soc.* **2010**, *132*, 15896.
5. E. R. Essinger-Hileman, D. DeCicco, J. F. Bondi, R. E. Schaak, *J. Mat. Chem.* **2011**, *21*, 11599.
6. D. J. Chakrabarti, D. E. Laughlin, *Bull. Alloy Phase Diagrams*, **1982**, *2*, 461.
7. N. A. Zarkevich, T. L. Tan, D. D. Johnson, *Phys. Rev. B* **2007**, *75*, 104203.
8. I. Nakamula, Y. Yamanoi, T. Imaoka, K. Yamamoto, H. Nishihara, *Angew. Chem. Int. Ed.* **2011**, *50*, 5830.

9. J. A. Creighton, D. G. Eadon, *J. Chem. Soc., Faraday Trans.* **1991**, *87*, 3881.
10. A. R West, in *Solid State Chemistry and its Application*, John Willey & Sons, **1984**.
11. L. Vegard, H. Dale, Z. *Kristallogr.* **1928** *67*, 148.
12. G. Ouyang, X. Tan, C. X. Wang, G. W. Yang, *Nanotechnology* **2006**, *17*, 4257.
13. J. A. Rodriguez, R. A. Campbell, D. W. Goodman, *J. Phys. Chem.* **1991**, *95*, 2477.

Chapter 4

Selective Hydrogenation of Nitroaromatics by Partially Oxidized Ir Nanoparticles

4.1 Introduction

Aniline derivatives are key precursors for pharmaceuticals, pesticides, dyes, and pigments [1]. Conventionally, these derivatives are synthesized by the catalytic hydrogenation of the corresponding nitroaromatics using NPs (NPs) of transition metals such as Pt, Pd, Rh, or Ru [2]. However, when the reactant contains other reducible groups, selectivity to obtain the desired aniline derivative is not satisfactorily high. It has been demonstrated that the selectivity of hydrogenation by mono- (Au, Ni, Ag, Ru, Pt, Ni) [3] or bi-metallic (Au-Ni) [4] NPs can be improved by employing specific metal oxide supports. The origin of the selectivity was ascribed to the selective adsorption of nitro group on the support. However, these catalysts usually require harsh conditions (323–430 K; 0.5–3MPa of H_2) leaving a room for further improvement.

Selective hydrogenation under milder conditions (273 K; 0.1 MPa of H_2) was reported using Ir NPs on a hydrous zirconia support [5]. Chloride-stabilized Ir NPs also hydrogenate acetone [6] and benzene [7] under mild conditions. These reports suggest that Ir is a potential candidate for active and selective hydrogenation catalysts of nitroaromatics. To test this hypothesis, I compared the catalytic performances of Ir NPs with those of NPs of other transition metals (Pd, Pt, Rh, and Au) for the hydrogenation of nitroaromatics containing –CHO, >C=O, –CN, and –Cl groups. For comparison purpose, all the NPs were stabilized by poly(*N*-vinyl-2-pyrrolidone) (PVP) and the average size was nearly constant (~2 nm). I found that Ir:PVP NPs yielded the best catalytic performance.

4.2 Experimental

4.2.1 Chemicals

Hexachloroiridic acid ($H_2IrCl_6 \cdot 6H_2O$), Palladium (II) chloride ($PdCl_2$), hexachloplatinic acid ($H_2PtCl_6 \cdot 6H_2O$), tetrachloroaurate ($HAuCl_4.4H_2O$), poly(N-vinylpyrrollidine) (PVP) (M_w: 40 kDa), sodium borohydride ($NaBH_4$), from Wako Pure Chemical Industries Ltd; Rhodium (III) acetate from Mitsuwa Pure Chemical Industries Ltd and H_2 gas (99.99 % purity) were purchased and used without further purification. Deionized water (18 MΩ cm) was used to prepare aqueous solutions.

4.2.2 Preparation

Ir:PVP was prepared the ethylene glycol (EG) reduction method: 0.1 mmol of H_2IrCl_6 and 2.0 mmol (in a monomer unit) of PVP (K30, MW = 40 kDa) were dissolved in 40 mL of EG. The pH of the solution was adjusted to be close to 5 by adding HCl, and the mixture was then stirred at room temperature for the complete dissolution of the precursor and PVP. The mixture was then stirred at 160 °C for 3 h under an argon atmosphere. During stirring, the solution gradually turned dark brown. After the dispersion was cooled to room temperature, 120 mL of water was added to lower the viscosity. The NPs were collected by passing the dispersion through a membrane filter with a cut-off molecular weight of 10 kDa.

Pt:PVP was also prepared by the EG reduction method. In this case, 0.3 mmol of H_2PtCl_6, 6.0 mmol (in a monomer unit) of PVP (K30, MW = 40 kDa) and 40mmol of NaOH were dissolved in 40 mL of EG. The mixture was stirred at room temperature for the complete dissolution of the precursor and PVP and then stirred at 140 °C for 3 h. The solution gradually turned dark black. After the dispersion was cooled to room temperature, 120 mL of water was added to lower

the viscosity. The NPs were collected by passing the dispersion through a membrane filter with a cut-off molecular weight of 10 kDa.

Au:PVP, Pd:PVP and Rh:PVP were prepared respectively from $HAuCl_4$, $PdCl_2$, and $RhCl_3$ by $NaBH_4$ reduction. To begin, 0.1 mmol of the precursors of each metal and 2.0 mmol (in a monomer unit) of PVP (K30, MW = 40 kDa) were dissolved in 40 ml of water, and 5 mL aqueous solution of $NaBH_4$ (10 eq. with respect to the metal) was then added to each precursor solution at 25 °C. The reaction mixtures were stirred vigorously for 30 min. The NPs were collected by passing the mixtures through a membrane filter with a cut-off molecular weight of 10 kDa.

4.2.3 Characterization

A. Transmission electron microscopy (TEM)

A drop of Ir:PVP dispersion (~0.4 mM) in ethanol was put on a hydrophobic film coated TEM grid and the solvent was dried naturally. Transmission Electron Microscope (JEM-2100F, JEOL) operated at 200 kV was used to study the morphology and the average size at different magnification ranging from 100,000–250,000.

B. Powder X-ray diffraction (XRD)

The finely powdered samples were put on a glass holder and slightly pressed with a glass slide to flatten the samples. Powder X-ray diffraction (XRD) profiles of the solid samples of M:PVP were measured by using a diffractometer (Miniflex, Rigaku) with a radiation source of Cu Ka (1.5418 Å) operated at 30 kV and 15 mA.

C. X-ray photoelectron spectroscopy (XPS)

The powdered Ir:PVP sample was dried in a lyophilizer (FDU-2200, Eyela) for 24 h and placed on the sample holder with a carbon conductive tape. The XP spectra were taken by using a spectrometer (PHI 5000 VersaProbe, ULVAC-PHI) with an energy resolution of 0.5 eV. The spectrum was calibrated using the C 1s peaks of PVP as internal standards. The XP spectra were fitted, by assuming 4 component of Gaussian peak. The peak positions were assigned keeping the similar differences in the binding energy in bulk phase.

D. X-ray absorption fine structure (XAFS)

Ir L_3 edge XAFS measurements were carried out at BL01B1 beam line at the SPring-8 facility of the Japan Synchrotron Radiation Research Institute (proposal no. 2012B1074). An Si(311) two-crystal monochromator was used for the incident beam. All spectra were recorded in transmission mode, and ion chambers were used for the I_0 and I detectors. The Ir:PVP solutions were placed between the ion chambers. Energy calibration was carried out using a Cu foil. Data analysis was carried out using the program REX2000 Ver.2.5.9 (Rigaku Co.). The EXAFS data were analyzed as follows. The χ spectra were extracted by removing the atomic absorption background using a cubic spline and were normalized to the edge height. The k^3-weighted χ spectra were Fourier transformed into the r space, using the Fourier transformation range 3.0-15 $Å^{-1}$. Curve fitting analysis was performed for the Ir-Ir bond. The curve fitting range was 2.1-3.1 Å. The passive electron factor (S_0^2) of 1 was used in this study. The phase and amplitude function of Ir-Ir bond were extracted from Ir metal (Space group: Fm3m, #ICSD: 41524) by calculation using FEFF8 [8]. The curve fitting results were summarized in Table S1.

4.2.4 General Procedure for Catalytic Hydrogenation

Hydrogenation reactions were carried out in a Teflon tube reactor settled inside a stainless steel autoclave. For a typical reaction, the ethylacetate solution of nitroaromatics (0.4 M, 1 mL) was added to the hydrosol (4 mL) of M:PVP (M = Ir, Pd, Pt, Rh, Au) containing 8 μmol of metal atoms. The biphasic system was then vigorously stirred at 25 °C under hydrogen (0.1 MPa). After 2 h, the organic layer was separated, and the products were analyzed by gas chromatography and gas chromatography–mass spectrometry.

4.3 Results and Discussion

Figure 4.1 shows representative TEM images of the M:PVP samples. The NPs in all samples were found to be monodisperse, and the average sizes of M:PVP were in the range of 1.6- 2.2 nm, from measuring the diameters of more than 200 particles. Powder XRD patterns revealed that all NPs have a face-centered cubic (fcc) crystal structure (Figure 4.2). The crystalline sizes were estimated from the Scherrer equation shown in Table 1, which are in good agreement with the TEM results.

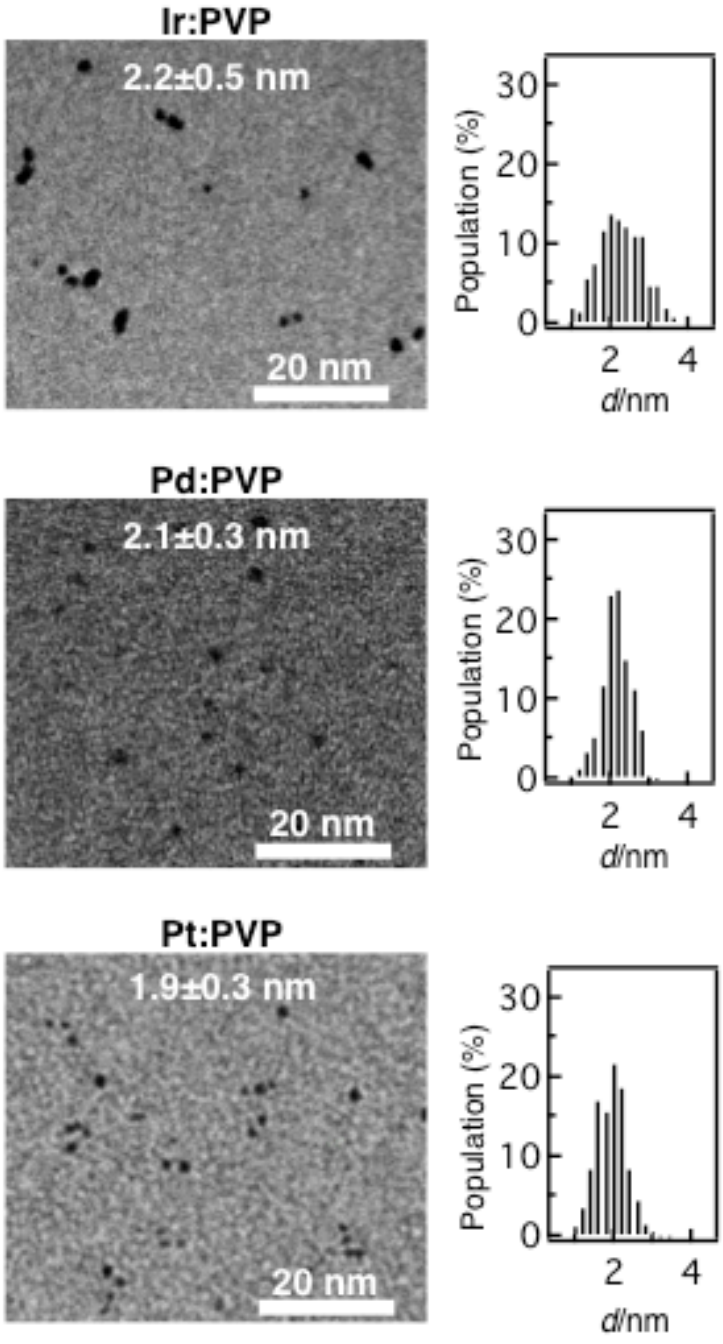
Ir:PVP
2.2±0.5 nm
20 nm
Population (%)
30
20
10
0
2
4
d/nm
Pd:PVP
2.1±0.3 nm
20 nm
Population (%)
30
20
10
0
2
4
d/nm
Pt:PVP
1.9±0.3 nm
20 nm
Population (%)
30
20
10
0
2
4
d/nm

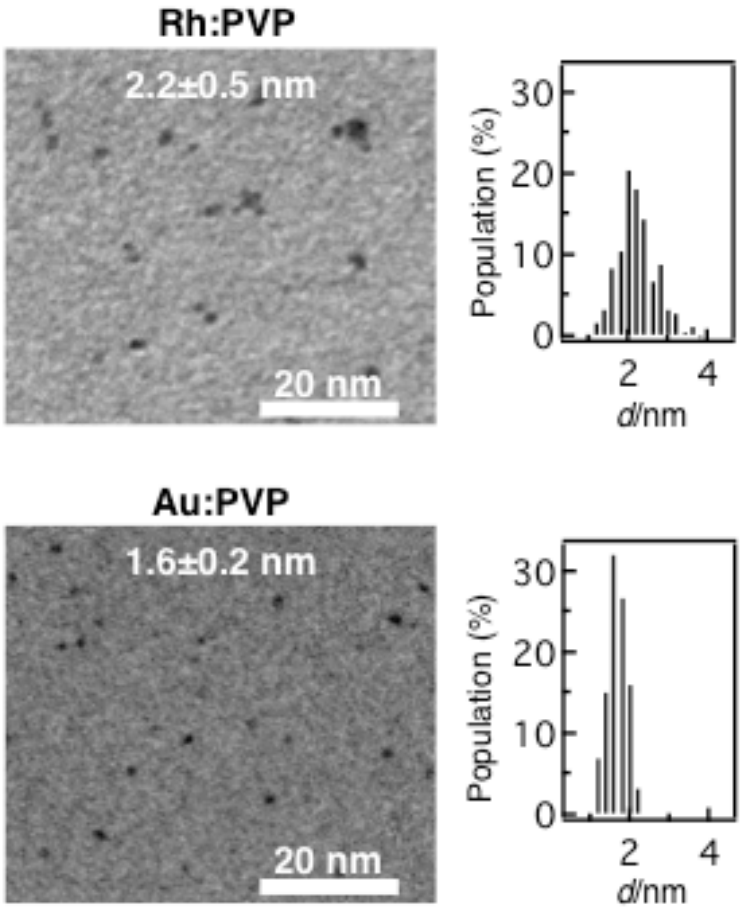

Figure 4.1. TEM images and size distribution of M:PVP.

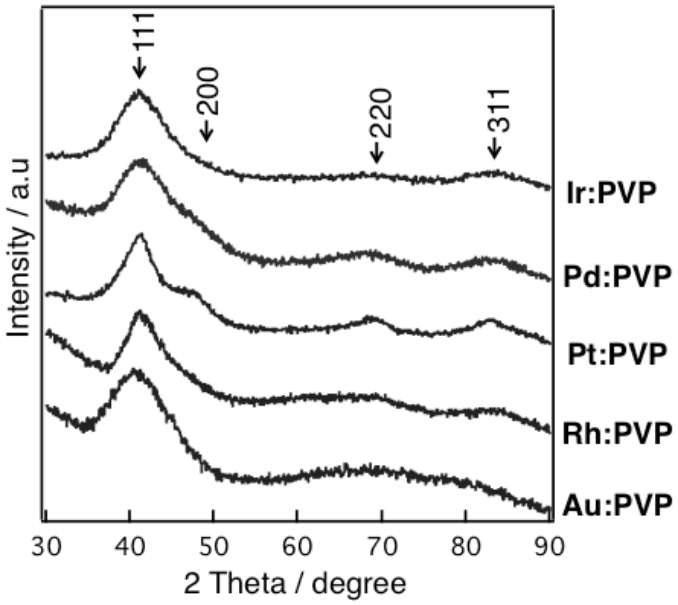

Figure 4.2. (a) XRD patterns of Fe_xCo_{100-x} NAs and (b) its expanded view at 011 position.

Table 4.1. Diameters of M:PVP NPs determined by TEM and XRD analyses.

M:PVP	Diameter	
	d_{TEM} (nm)	d_{XRD} (nm)
Ir	2.2	2.1
Pd	2.1	1.6
Pt	1.9	1.8
Rh	2.2	2.0
Au	1.6	1.5

The catalytic performance of M:PVP (M=Ir, Pd, Pt, Rh, Au) was first compared using hydrogenation of 4-nitrobenzaldehyde (**1**) as a test reaction. The results of the catalytic tests are summarized in Figure 3. In all cases, partially reduced species, 4-aminobenzaldehyde (**2**), and fully reduced species, 4-aminobenzyl alcohol (**3**), were obtained as the products. 4-Nitrobenzyl alcohol was not produced. Conversions of **1** under these mild conditions were nearly

100 % for all the catalysts except Au:PVP. However, selectivity towards **2** was strongly dependent on the metal: Ir NPs showed the highest selectivity. The substrate scope for Ir:PVP was investigated for the hydrogenation of nitroaromatics containing >C=O, –CN and –Cl functional groups. All the nitroaromatics were reduced very efficiently and selectively to the corresponding aniline compound, while the other functional groups remained intact (Table 2.2).

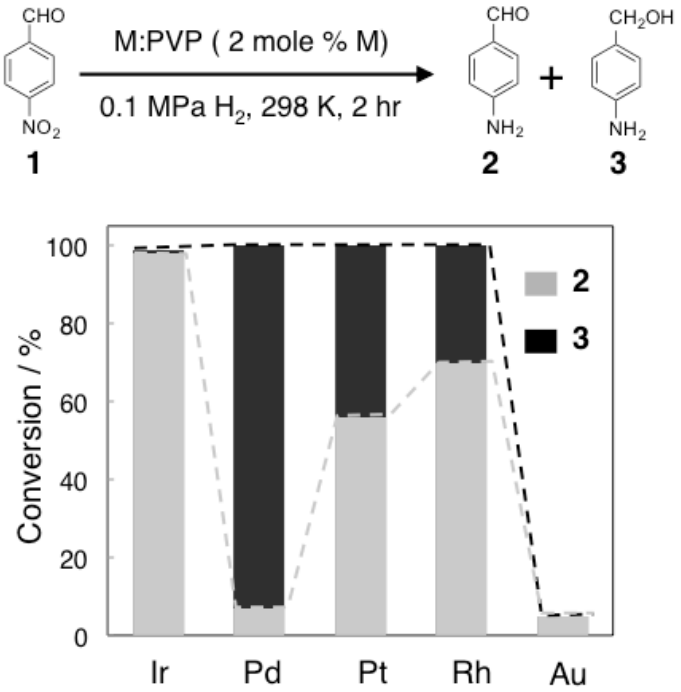

Figure 4.3. Catalytic hydrogenation of 4-nitrobenzaldehyde by PVP-stabilized metal NPs.

Table 4.2. Catalytic hydrogenation of nitroaromatics by Ir:PVP.

Entry	Substrate	Conv. %	Product	Select. %
1	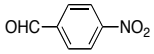	99	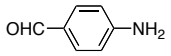	99
			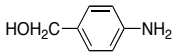	1
2	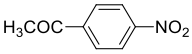	100	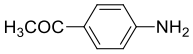	100
3	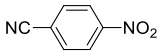	95	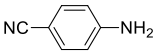	100
4	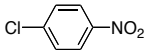	100	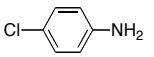	99
			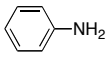	1

To reveal the origin of the high selectivity of Ir:PVP, time courses of the reactions were studied for Ir:PVP and Pt:PVP (Figure 4.4). In the case of Ir:PVP, selectivity to the fully reduced product **3** did not evolve even after **1** was completely converted to **2**. In contrast, selectivity to **3** by Pt:PVP gradually increased as the reaction time lengthened. This suggests that selectivity to **2** by Ir:PVP(B) is not determined kinetically, but by a low reducing ability of Ir:PVP toward **2**.

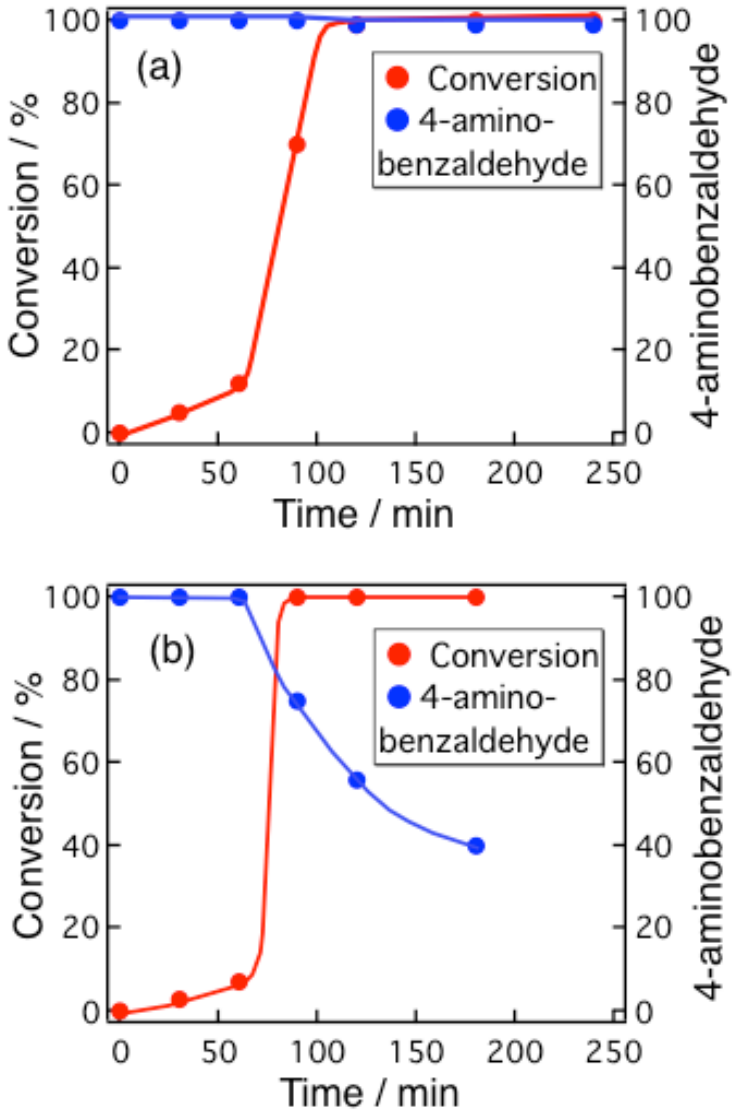

Figure 4.4. Time course of the hydrogenation of 4-nitrobenzaldehyde by the (a) Ir:PVP and (b) Pt:PVP NPs.

Then, more detail structural characterization for Ir:PVP were carried out by XAFS measurement and XP to reveal the origin of the high selectivity of Ir:PVP. Figure 4.5 shows the Fourier-transformed EXAFS spectra of Ir:PVP along with IrO_2 and bulk Ir and corresponding EXAFS oscillation spectrum. The peaks in the 1.45-1.85 and 2.23–2.95Å ranges were assigned to the Ir-O and Ir-Ir shells, respectively. The average coordination number (*CN*) of Ir-Ir is 9.8. The *CN*

values are consistent with those estimated assuming a cuboctahedral morphology 9.63 for Ir_{309} (~2.2 nm).

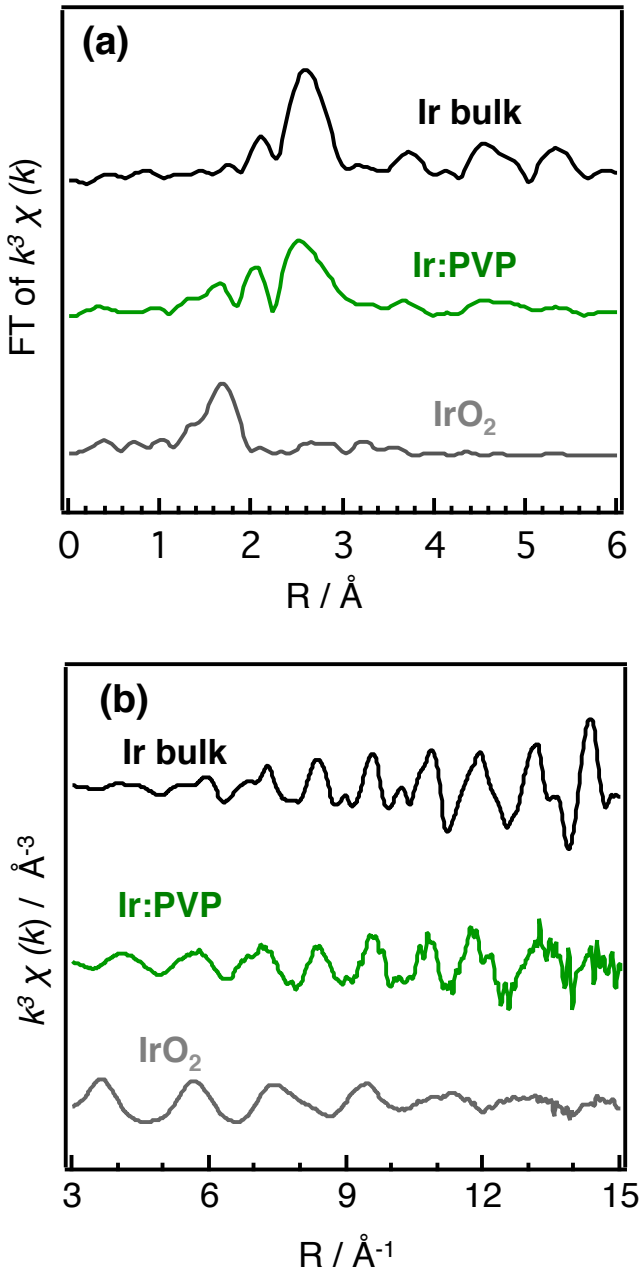

Figure 4.5. (a) Fourier transformed EXAFS spectra of Ir bulk, Ir:PVP, and IrO_2 and (b) Corresponding EXAFS oscillation.

Figure 4.6 shows the XP spectrum of Ir:PVP around the Ir 4f region. The XP spectra were analyzed by the least-square method assuming four bands with Gaussian profiles for $4f_{7/2}$ and $4f_{5/2}$ bands of Ir(0) and IrO_2. The binding energies

of Ir $4f_{7/2}$ and $4f_{5/2}$ peaks were obtained to be 59.7–59.8 and 62.7–62.8 eV, respectively, which are slightly smaller than the corresponding values of the bulk (60.8 and 63.8 eV) [9]. This can be attributed to electron donation from the PVP, which makes the NPs slightly negatively charged as in the case of Au:PVP [10] and Pt:PVP [11]. In addition, peaks assignable to IrO_2 were detected at 60.7-60.8 and 64.5 eV for $4f_{7/2}$ and $4f_{5/2}$, respectively, which are also slightly smaller than the corresponding bulk values [5, 12]. The relative population of IrO_2 component is 11 %.

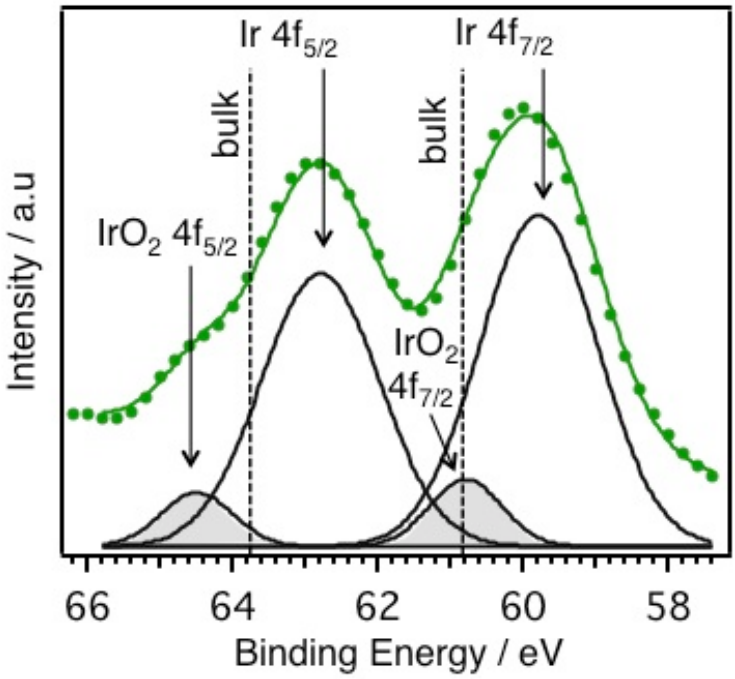

Figure 4.6. XP spectra of Ir:PVP. The experimental data (dotted points) and deconvoluted spectra (black curves) are offset for clarity.

To understand the structure of the partially oxidized Ir NPs I calculated the population of surface atoms for a 2.2 nm NPs assuming cuboctahedral model. According this model, ~57 % atoms are surface atoms. In order to form an oxide shell metal core type structure, nearly 57 % Ir atoms should be oxidized. But only 11 % Ir atoms were found to be oxidized from XP analysis. Therefore,

finally I conclude that small domain of IrO_2 is randomly located on the surface of the iridium (IrO_2/Ir) as shown in Figure 4.7.

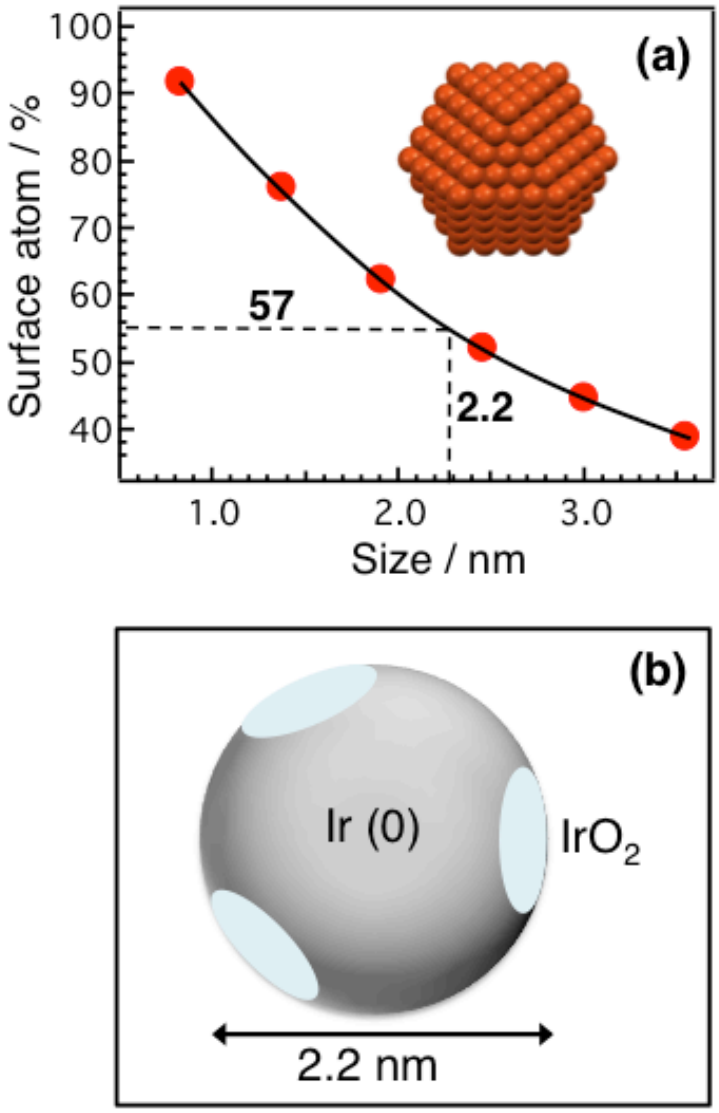

Figure 4.7. (a) Surface atoms ratio as function of size for cuboctahedral model. (b) Proposed the structure of Ir NPs.

Based on the partially oxidized IrO_2/Ir structure I proposed the possible reaction mechanism in Figure 4.8. According to the previous reports [3], selective reduction of nitroaromatics into the corresponding aniline derivatives was ascribed to the preferential adsorption of the nitroaromatics on the metal oxide support via the NO_2 group. In the framework of this model, I can speculate

that nitroaromatic molecules are preferentially adsorbed onto the IrO_2 site through the NO_2 group. On the other hand, atomic hydrogens are possibly formed on the Ir NP surface by dissociation of H_2 according to recent observations of hydrogen storage by Ir NPs [13]. Thus, the efficient and selective hydrogenation by Ir:PVP can be ascribed to both preferential adsorption of the NO_2 group onto the oxidized area and activation of the hydrogen on the non-oxidized area. Ir NPs whose surfaces are partially oxidized can be viewed as an inverse system of conventional supported metal catalyst [3,14]. The unique feature of such an inverse system is that the interfacial area between the metal NPs and metal oxide support can be enhanced. A similar idea was recently demonstrated by Mitsudome *et al.* for a nanocomposite comprising an Ag NP core and a shell of CeO_2 NPs [15].

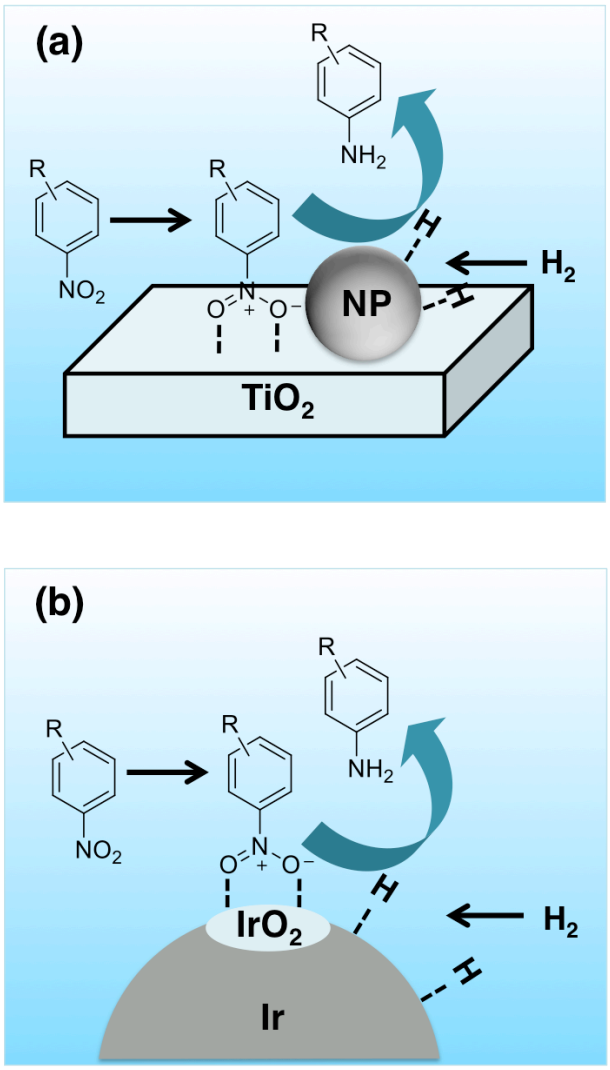

Figure 4.8. Proposed reaction mechanism in previous literature (a) and in this work (b).

A technical problem in the application of colloidal NPs for catalysis is the recovery of NPs for reuse. The aqueous–organic biphasic system employed here is suitable for easy recovery of the catalyst, and the reusability of Ir:PVP was tested for up to 3 cycles of hydrogenation of **1**. The catalysts were collected by separating the aqueous layer from the reaction mixture so that they could be used in the next run. The catalytic performance of the third run was comparable to that of the first run (Figure 4.9), suggesting that colloidal Ir:PVP dispersed in water can be reused without the loss of catalytic performance. The size of the Ir

catalyst after reuse was measured by TEM, which revealed that the particle size and distribution did not change appreciably from those of the original NPs (Figure 4.10).

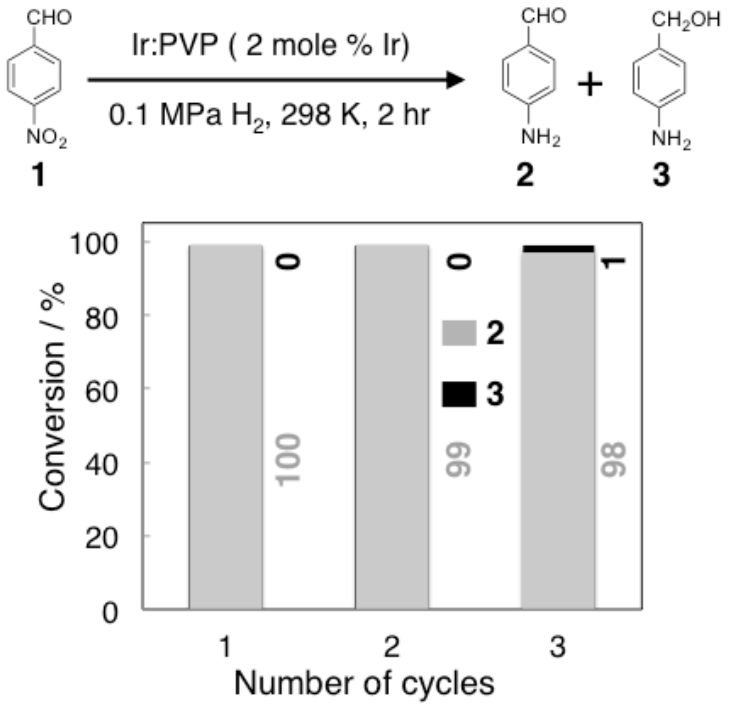

Figure 4.9. Catalytic hydrogenation of 4-nitrobenzylaldehyde as a function of the number of reuse cycles by Ir:PVP.

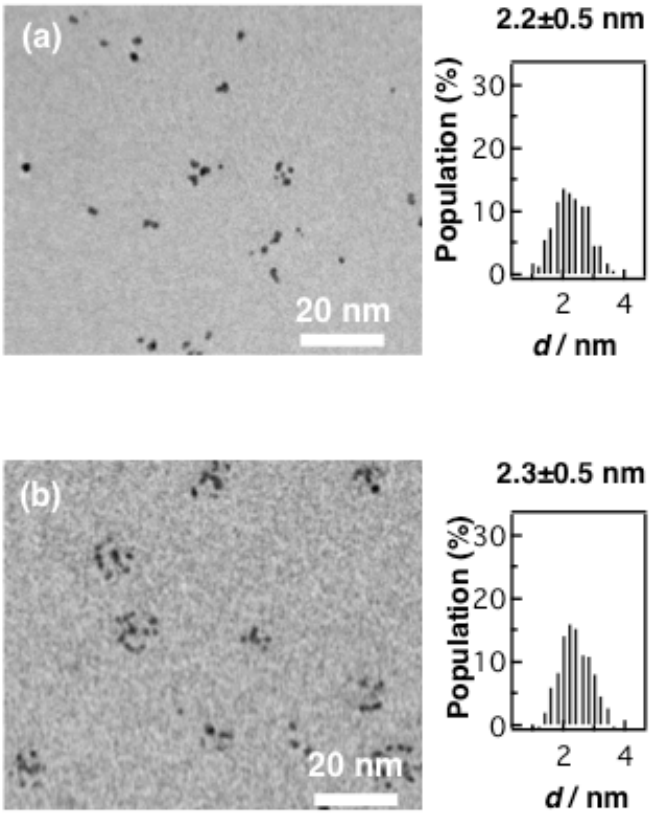

Figure 4.10. TEM images of Ir:PVP (a) before and (b) after catalytic hydrogenation of 4-nitrobenzylaldehyde.

4.4 Summary

In summary, I have demonstrated the hydrogenation of nitroaromatics by colloidal Ir:PVP NPs under mild conditions (298 K and 0.1 MPa of H_2) and obtained aniline derivatives with >C=O, –CHO, –CN, and –Cl functional groups from the corresponding nitroaromatics. Ir:PVP showed a higher selectivity than the other metal NPs stabilized by PVP due to presence of a partially oxidized area on the Ir NPs.

References

1. (a) T. Kahl, K.-W. Schröder, F. R. Lawrence, W. J. Marshall, H. Höke, R. Jäckh, in *Ullmann's Encyclopedia of Industrial Chemistry,* Wiley- VCH Verlag GmbH & Co. KGaA, **2000. (**b) G. Wegener, M. Brandt, L. Duda, J. r. Hofmann, B. Klesczewski, D. Koch, R.-J. Kumpf, H. Orzesek, H.-G. Pirkl, C. Six, C. Steinlein, M. Weisbeck, *Appl. Catal. A* **2001,** *221,* 303.
2. (a) M. Tafesh, J. Weiguny, *Chem. Rev.* **1996,** *96,* 2035. (b) R. S. Downing, P. J. Kunkeler, H. van Bekkum, *Catal. Today* **1997,** *37,* 121.
3. (a) Corma, P. Serna, *Science* **2006,** *313,* 332. (b) M. Boronat, P. Concepción, A. Corma, S. González, F. Illas, P. Serna, *J. Am. Chem. Soc.* **2007,** *129,* 16230. (c) A. Corma, P. Serna, P. Concepción, J. J. Calvino, *J. Am. Chem. Soc.* **2008,** *130,* 8748. (d) K. Shimizu, Y. Miyamoto, T. Kawasaki, T. Tanji, Y. Tai, A. Satsuma, *J. Phys. Chem. C* **2009,** *113,* 17803. (e) K.-i. Shimizu, Y. Miyamoto, A. Satsuma, *J. Catal.* **2010,** *270,* 86. (f) M. Makosch, W.-I. Lin, V. c. Bumbálek, J. Sá, J. W. Medlin, K. Hungerbúhler, J. A. van Bokhoven, *ACS Catal.* **2012,** *2,* 2079.
4. F. Cárdenas-Lizana, S. Gómez-Quero, G. Jacobs, Y. Ji, B. H. Davis, L. Kiwi-Minsker, M. A. Keane, *J. Phys. Chem. C* **2012,** *116,* 11166.
5. G.-Y . Fan, L. Zhang, H.-Y . Fu, M.-L. Y uan, R.-X. Li, H. Chen, X.-J. Li, *Catal. Commun.* **2010,** *11,* 451.
6. S. Özkar, R. G. Finke, *J. Am. Chem. Soc.* **2005,** *127,* 4800.
7. E. Bayram, M. Zahmakıran, S. Özkar, R. G. Finke, *Langmuir* **2010,** *26,* 12455.
8. A.L. Ankudinov, B. Ravel, J.J. Rehr, S.D. Conradson, *Phys. Rev. B* **1998**, *58*, 7565.

9. T. S. Marinova, K. L. Kostov, *Surf. Sci.* **1987,** *181,* 573.

10. H. Tsunoyama, N. Ichikuni, H. Sakurai, T. Tsukuda, *J. Am. Chem. Soc.* **2009,** *131,* 7086.

11. M. J. Hossain, H. Tsunoyama, M. Yamauchi, N. Ichikuni, T. Tsukuda, *Catal. Today* **2012,** *183,* 101.

12. (a) J. Riga, C. Tenret-Noel, J.J. Pireaux, R. Caudano, J.J. Verbist, Gbillon *Phys. Scripta* **1977,** 16, 35. (b) A.K. Shukla, A.M. Kannan, M.S. Hegde, J. Gopalakrishnan, *J. Power Sources* **1991,** 35, 163.

13. H. Kobayashi, M. Yamauchi, H. Kitagawa, *J. Am. Chem. Soc.* **2012,** *134,* 6893.

14. (a) A. Noujima, T. Mitsudome, T. Mizugaki, K. Jitsukawa, K. Kaneda, *Angew. Chem. Int. Ed.* **2011,** *50,* 2986. (b) Noujima, T. Mitsudome, T. Mizugaki, K. Jitsukawa, K. Kaneda, *Chem. Commun.* **2012,** *48,* 6723.

15. T. Mitsudome, Y. Mikami, M. Matoba, T. Mizugaki, K. Jitsukawa, K. Kaneda, *Angew. Chem. Int. Ed.* **2012,** *51,* 136.

Chapter 5
Concluding Remarks

Other than size and shape and composition, mixing mode are important structural parameters to control the novel properties of binary NPs. In this work, structure regulated novel binary NPs were prepared and their magnetic and catalytic properties investigated.

Several difficulties arise in preparing FeCo NAs to poor controllability of structure parameters such as inhomogeneous mixing, poor crystallinity and oxidation. In chapter 2, I demonstrated that these difficulties in preparation of FeCo NAs were overcome by using hydrogenation reduction method of PEG stabilized phase-separated FeCo oxide composite. Here, the hydrogen played a dual role: (1) as a reducing agent to reduce the oxide phase to metallic phase; (2) promotion of atomic diffusion for homogeneous mixing. The homogenous mixing promoted formation of a highly crystalline structure of periodic lattice fringe. The FeCo NAs were oxidation resistant due to formation of carbon layer on the surface by the burning of the PEG. The homogeneous mixing, high crystallinity and stability against oxidation reflected in the magnetic properties of FeCo NAs. The homogenous mixing and good crystallinity enhance the electronic interaction between Fe and Co. Therefore, high saturation magnetization was observed in $Fe_{70}Co_{30}$ NA, which is comparable to bulk $Fe_{70}Co_{30}$ alloy.

In conclusion, hydrogen reduction method is useful for preparing homogeneously mixed NAs even from a phase-separated structure and minimizing the sintering of NPs.

Scheme 5.1 Role of hydrogen to prepare solid solution alloy.

Solid solution alloys may exhibit new properties through the modification of the electronic structures. Limited numbers of solid solution structures have been reported according to phase diagram in bulk state. Thus, new solid solution structures are required in order to explore new properties. Phase diagram in bulk state does not predict the formation of solid solution structure of RhCu. In chapter 3, I demonstrated the preparation of solid solution RhCu NAs by a co-reduction of two metal ions in presence of PVP. The lattice constants of these NAs clearly revealed that structures were solid solution. It can be conclude that the solid solubility of two immiscible metal can be increased drastically in nano-size.

These NAs acted as active and selective catalyst for the hydrogenation of 4-nitrobenzaldehyde under 0.1 MPa of H_2 at 298 K. However, one of the fundamental issues still remains: the origin of high selectivity. I speculated that polarized $Rh^{\delta-}Cu^{\delta+}$ surface is the possible reason for high selectivity. This work is expandable to this end by the controlling of surface composition. An ordered structure is featured by a fixed surface composition. Therefore, I envision the development of ordered structure of the RhCu.

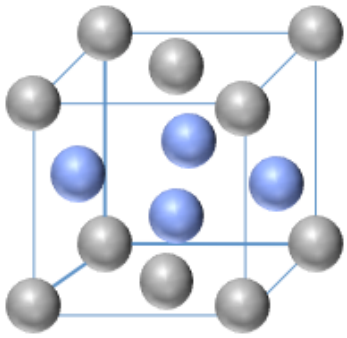

Figure 5.1 Possible ordered structure of RhCu

Although bulk Ir is oxidation resistant, I found that Ir NPs are slightly oxidized. Detailed structural analysis revealed that small IrO_2 domains are randomly located on the surface of Ir NPs. Among the different transition metal (Ir, Pd, Pt, Rh, Au) NPs protected by PVP (M:PVP) of ~2 nm size, Ir:PVP showed the best selectivity at high conversion under 0.1 MPa of H_2 at 298 K. Then, I deliberated to find out the origin of selectivity. Previous literature suggested that selective hydrogenation occurs through a cooperative effect between metal NPs and oxide support at the interfacial area of NPs and support. Similar cooperative effect occurs in IrO_2/Ir giving a selective reduction of NO_2 group where NO_2 group is selectively adsorbed on IrO_2 phase and molecular hydrogen dissociates on Ir (0) phase. This partially oxidized Ir NPs (oxide/metal) can be classified as an inverse system of conventional catalyst system (metal/oxide). As the size of Ir NP is very small of 2.2 nm, the interfacial area between oxide phase and metallic phase is greatly enhanced.

This oxide/metal structure of Ir NPs inspire me to design an oxide/metal structure at controlled composition for other high active metal like Pd, Pt. It can be expect that the extension of this idea to other metal will open a new window in the field of catalysis.

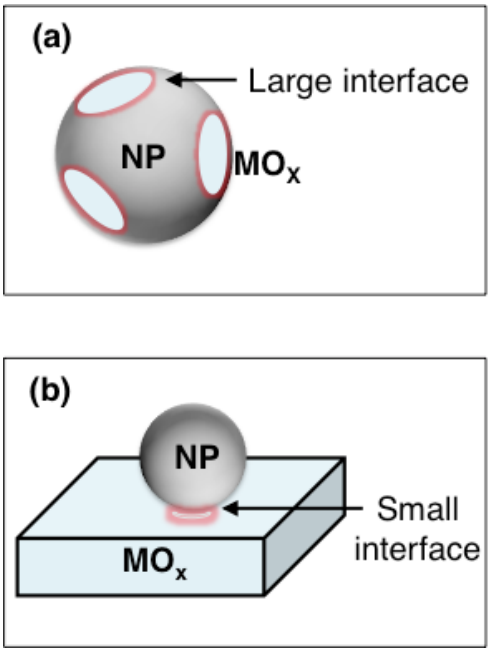

Figure 5.2 (a) Large interfacial area in new type of catalyst (oxide/metal), (b) small interfacial area in conventional catalyst metal/oxide).

List of Publications

1. Enhanced Magnetization in Highly Crystalline and Atomically Mixed bcc Fe-Co Nanoalloys Prepared by Hydrogen Reduction of Oxide Composites
M. J. Sharif, M. Yamauchi, S. Toh, S. Matsumura, S.-i. Noro, K. Kato, M. Takata, T. Tsukuda, *Nanoscale* **2013**, *5*, 1489-1493.

2. Selective Hydrogenation of Nitroaromatics by Colloidal Iridium Nanoparticles
M. J. Sharif, P. Maity, S. Yamazoe, T. Tsukuda, *Chem. Lett.* **2013,** (In press). DOI: http://dx.doi.org/10.1246/cl.130333

(Publication 1 and 2 has been reproduced in this thesis in chapter 2 and 4 respectively, with little modification)

Acknowledgement

I find great pleasure to acknowledge with sincere appreciation to my supervisor, Prof. Tatsuya Tsukuda who had given me the chance to join as a PhD student at Hokkaido University and later he gave me the chance to work in his new Lab at The University of Tokyo. I really developed my skills and knowledge by the frequent discussion, proper guidance, and constructive suggestions throughout the time my study.

I acknowledge with deep sense of gratitude to former Associate Prof. Miho Yamauchi who taught me at the initial stage of my study. I also developed my experimental skills and way of thinking by her active guidance and hearty cooperation.

I am grateful to Prof. Atsushi Fukuoka who accepted me officially as a student in his group and for his valuable comments and suggestion during this work.

I am also grateful to former Ast. Prof. Hironori Tsunoyama, Asso. Prof. Kiichiro Koyasu. Ast. Prof. Seiji Yamazoe, Dr. P. Maity, Dr. Xie, Dr. J. Nishigaki, Dr. HM Jakir and all other member of Tsukuda lab for their help and suggestion during my work.

I want to express my gratitude to Hokkaido University authority for choosing me as candidate for the President Scholarship. A lot of thanks to former GCOE project and AGS program for funding me up to the half of the period of my study. Also thanks to Japan Student Services Organization (JASSO) for the financial support from October 2012.

Finally, I would like to give special thanks to my wife Kohinur Nahar who

always inspired me specially when I face any difficulty either in my research work or in daily life. She always kept patience and managed the daily life very smoothly when I was busy in my research work.